Academic year
2023 - 2024

Bachelor Thesis

Non-perturbative Quantum Chromodynamics Effects in Drell-Yan Lepton Pair Production at the Large Hadron Collider

Amine Ben Mahmoud

Bachelorproef
Bachelor of Science in de fysica

Supervisor
Prof. Dr. Francesco Hautmann, UAntwerpen

University of Antwerp
Faculty of Science

Disclaimer Bachelorproef

This document is in accordance with the master thesis regulations and the Code of Conduct. It has been reviewed by the supervisor and the attendant.

Abstract

The production of lepton pairs via the Drell-Yan (DY) mechanism of electroweak vector boson exchange is one of the most accurately measured processes in high-energy proton-proton collisions at the Large Hadron Collider (LHC). It provides key insights into proton structure, precision electroweak observables, and possible extensions of the Standard Model of Particle Physics. In the region of small transverse momenta of the lepton pair, important strong-interaction effects arise due to the non-perturbative physics of Quantum Chromodynamics (QCD), the quantum field theory describing the interactions of quarks and gluons (partons). The DY transverse momentum cross section can be described in QCD as a convolution of partonic scattering functions, calculable in perturbation theory, and transverse momentum-dependent (TMD) parton densities, evolving with the energy scale according to parton-branching evolution equations, and including non-perturbative distributions of the intrinsic transverse momenta k_T of the partons. In this thesis, we apply existing computer codes for the scattering functions and the TMD parton-branching evolution as well as non-perturbative parameterizations for intrinsic-k_T distributions to obtain theoretical results for DY cross sections. We compare our results with experimental measurements of DY transverse momentum spectra carried out recently at the LHC over a wide range of lepton-pair invariant masses. We find good agreement of theory with experiment and perform fits of non-perturbative intrinsic-k_T parameters to experimental data. In particular, we study the interplay of this parameter with the resolution scale used in the branching evolution for soft-gluon radiation. Our results are consistent with average values of intrinsic-k_T on the order of 1 GeV, and mild dependence on the invariant mass.

Contents

Acknowledgments

I am grateful to Francesco Hautmann for his invaluable assistance whenever I had questions about the theory and giving me the needed sources to better understand this complex topic. For the data analysis part of the thesis, I received exceptional guidance from Aleksandra Lelek, which greatly enhanced my understanding of how to operate Cascade3 and also taught me a lot about Linux, an area where I previously had no experience. I encountered no issues in obtaining my results and plots under her guidance. I would also like to express my gratitude to Pierre Van Mechelen, who provided excellent lessons throughout my bachelor years on particle physics, which significantly aided my understanding of complex topics. This thesis would not have been possible without the support of these individuals, and I am deeply thankful for their contributions.

I would also like to note that this is my first time writing such a comprehensive project in English, and Chat-GPT has been tremendously helpful in refining the language used in the thesis.

Finally, I want to express my gratitude once more to all the individuals mentioned above for making it possible for me to work on this thesis. It has been a wonderful experience and a fascinating topic. Although many concepts in the thesis, like quantum field theory, are still beyond my current level of knowledge, I have striven to produce a readable work, and I feel my understanding has significantly deepened. I am eager to explore these topics further in my Master's program. This journey would not have been feasible without the guidance of Francesco Hautmann and Aleksandra Lelek. Thank you for giving me the opportunity to work on this project.

Introduction

The study of elementary particles focuses on the smallest components of the universe and their interactions. These tiny particles and fundamental forces are encapsulated within a framework called the Standard Model, which comprises several theories based on quantum field theory and relies on gauge symmetries associated with Lie groups. The primary focus of this research is the strong interaction, with its associated theory being quantum chromodynamics (QCD). The Large Hadron Collider at CERN plays a crucial role in exploring these concepts. Specifically, we will examine high-energy hadron collisions, which often involve protons accelerated to extremely high speeds before colliding and interacting with each other. The information gathered from observing these processes will help us understand how quarks and the strong force work within these protons.

In Chapter 1, we will introduce some general definitions that form the building blocks of particle physics. This chapter initially covers the types of particles that exist, the fundamental forces, and introduces properties that differentiate the particles. Once this is done, we will introduce an important concept, the Feynman diagrams, which will provide us with a good visualization of these interactions. After that, there will be a brief section about the machinery at CERN. Finally, we will delve into the details of the strong force, which will serve as a foundation for the theory-intensive part of the thesis.

In Chapter 2, which is also an introductory chapter, we aim to establish a solid, albeit basic, understanding of quantum chromodynamics (QCD). We'll discuss how to account for color charge mathematically and derive Feynman rules for strongly interacting Feynman diagrams. Subsequently, we'll examine an important experiment, deep inelastic scattering, where we derive the structure functions that provide insights into the internal structure of hadrons.

Despite being the most accurate theory for describing the strong interaction, QCD is challenging because particle interactions inside hadrons occur in a regime where direct perturbative calculations often fail. Fortunately, we can utilize the collinear factorization theorem, which will also be briefly explained in Chapter 2. This theorem combines two kinds of objects: one that describes the high-energy aspect, and another that covers the low-energy, large-distance, or long-timescale aspect. The latter is the collinear parton distribution function (PDF), which describes how partons are distributed within a given hadron. These functions depend on the fraction of the longitudinal momentum of the hadron that is carried by the parton, as well as on the energy scale. We will also address transverse momentum in Chapter 3. Before that, however, we will introduce the strong coupling using the renormalization scheme.

Chapter 3 will delve into an algorithm that incorporates the transverse momentum of partons, utilizing transverse momentum-dependent parton distribution functions (TMD PDFs) and corresponding TMD factorization theorem. These TMD PDFs also account for the transverse momentum of the parton. The dependence of PDFs on the energy scale is calculated with evolution equations. The DGLAP equation handles this for collinear PDFs, but a new formulation is needed for TMD PDFs, which will be derived in Chapter 3 and will depend on the intrinsic-k_T, which is the non-perturbative transverse momentum parameter. As previously stated, hadron collisions are very important, and we will be examining a specific process in Chapter 4, namely the Drell-Yan process, which is a hadronic collision that produces a lepton pair. The idea here is to start with a straightforward example to calculate the cross-section, and then apply more complex perturbative QCD corrections to the Drell-Yan process to derive an expression

that matches the DGLAP evolution equation. To conclude this section, we will delve into the more phenomenological part of the thesis and discuss the method and program used to calculate the Drell-Yan transverse momentum (p_T) using the transverse momentum distribution dataset obtained by the CMS detector at CERN.

Finally, in chapter 5 we will investigate the dependence of our theoretical predictions for the DY transverse momentum on the non-perturbative intrinsic-k_T parameter, and we will compare our results with experimental measurements by performing fits of the intrinsic-k_T parameter to data. The focus here is to examine the influence of varying the range of p_T on various q_s values while adjusting the mass of the lepton pair and observing the results. These q_s values are directly related to the intrinsic-k_T, where k_T represents the transverse momentum of a parton, and q_s is a parameter that provides a measure of the average sideways motion of the partons. This study has been done before with a fixed or constant resolution scale, which is a function defining the threshold at which parton emissions in a parton shower are considered significant enough to resolve during the evolution of the parton shower. In this study we want to try the same calculations, but this time we will be using a dynamical resolution scale that will be dependent on the minimum transverse momentum needed for transmission of particle.

1 Fundamentals of Particle Physics

In this thesis, we delve into the realm of particle physics, the branch of physics concerned with the study of fundamental particles and the forces governing the universe. A fundamental (or elementary) particle is one that cannot be subdivided into smaller entities; these particles are the most basic constituents of matter and energy. The theoretical framework that categorizes these fundamental particles and describes the interactions between them is known as the Standard Model of particle physics. The model covers three main forces: electromagnetism, weak nuclear force, and strong nuclear force, but it leaves out gravity. This is because we don't fully understand how gravity fits in with the other forces yet. So, we won't be talking about gravity in this thesis either.

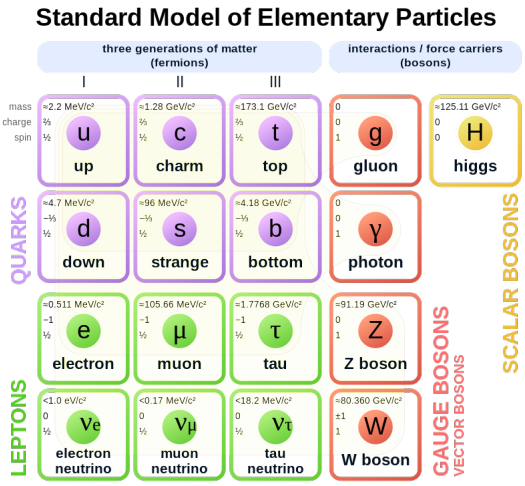

Figure 1.1: Simplified diagram of the Standard Model: This chart categorizes the fundamental particles into quarks, leptons, and bosons, showing their basic properties [1].

With these fundamental forces, particles can interact with each other and to conceptualize the interactions between particles, one might use the analogy of two individuals exchanging letters, where the exchange is facilitated by a postman representing one of the fundamental forces. The nature of the letter (or the force being conveyed) determines which type of interaction is occurring. The mediating particles, or gauge bosons, act as the carriers of these forces, as summarized below,

Interaction	Mediating Particle
Electromagnetic	Photon (γ)
Weak	W/Z-boson (W^+, W^-, Z^0)
Strong	Gluons

Table 1.1: Overview of fundamental forces in, detailing the types of interactions (Electromagnetic, Weak, Strong) and their corresponding mediating particles (Photon, W/Z Bosons, Gluons), essential for particle interactions.

Table 1.1 gives a quick look at the main interactions and the particles involved in them. The fundamental particles known as fermions can be categorized into two groups: quarks and leptons. Quarks form protons, neutrons, and other hadrons, while leptons include electrons and neutrinos. Quarks are divided into six flavors (or types), while leptons are divided into three flavors based on their properties, which we'll discuss later. A key difference between quarks and leptons is that quarks interact with the strong nuclear force, while leptons do not.

The distinction between bosons and fermions can be understood through their spin, a fundamental property further elaborated upon later. Bosons possess integer spins (0, 1, 2, ...), whereas fermions have half-integer spins (1/2, 3/2, 5/2, ...). Delving deeper, quantum mechanics teaches us that swapping the positions of two identical particles can result in two scenarios [2],

$$\begin{cases} |\psi'\rangle = |\psi\rangle \\ |\psi'\rangle = -|\psi\rangle \end{cases} \tag{1.1}$$

This behavior underpins a more general principle distinguishing the two: the Pauli Exclusion Principle, which asserts that no two fermions can occupy the same quantum state simultaneously. This principle explains, for instance, why an atomic orbital can host only two electrons, each with an opposite spin. In contrast, bosons are not subject to this principle, allowing an unlimited number of bosons to share a quantum state. This characteristic enables phenomena such as Bose-Einstein condensates (which is a whole other topic) [2].

The final particle we have yet to discuss is the Higgs boson. This particle is associated with the Higgs field, which essentially explains how fundamental particles acquire mass. The principle is straightforward: particles that interact more intensely with the Higgs field end up being more massive. This overview of the Higgs boson is quite brief, and delving deeper into this topic would take us into complex theories and mathematics beyond the scope of this thesis.

1.1 Exploring Particle Properties

To distinguish among these more specific particles, we rely on properties that help identify them,

- In particle physics, the electronvolt (eV) is the standard unit of energy, defined as the energy gained by an electron when it moves through an electric potential difference of one volt. **Masses** are measured in GeV/c², stemming from Einstein's equation $E = mc^2$, where $1\,\text{GeV} = 10^9\,\text{eV} = 1.6 \times 10^{-10}\,\text{Joule}$. The only particle that doesn't have mass is the photon [3].

- **Electric charge**: Charges are measured in units equivalent to the charge of a proton, which is positive and denoted by $+1$. An electron has a charge of -1 while neutrally charged particles, like neutrinos, have a charge of 0. Quarks possess fractional charges, such as the up quark with a $+\frac{2}{3}$. In SI units, the electric charge of the proton is 1.6×10^{-19} Coulombs [4].

- **Spin**: This intrinsic angular momentum differentiates particles further. While analogies often depict particles as spinning spheres, spin is a complex quantum mechanical attribute not indicative of physical spinning. Fermions (quarks and leptons) have a spin of $1/2$, while bosons (force carriers) have a spin of 1.

- **Flavor**: This characteristic helps differentiate between types of elementary particles. Particles with the same flavor are mostly identical but can vary in mass. Flavor is crucial when discussing quarks and leptons. There are six quark flavors: Up (u), Down (d), Charm (c), Strange (s), Top (t), and Bottom (b); and three lepton flavors: Electron (e), Muon (μ) and Tau (τ). Flavor-changing

events can occur through weak interactions, allowing particles to switch from one flavor to another [5].

Having outlined some fundamental particle properties, we can now delve into the concept of antimatter. Each type of particle has a corresponding antiparticle, typically denoted with a bar over the particle's symbol (for instance, the antielectron or positron is represented as $\bar{e}$). These antiparticles possess the same mass and spin as their particle counterparts but have opposite electric charges. In the case of neutral particles, they are considered to be their own antiparticles.

1.2 Feynman Diagrams

An essential tool developed by physicist Dr. Richard Feynman is the Feynman diagram. These diagrams visually represent the mathematical expressions that describe the behavior and interactions of subatomic particles. Due to the complexity of these interactions, Feynman diagrams provide a way to simplify and visualize what would otherwise be complicated and abstract equations [6].

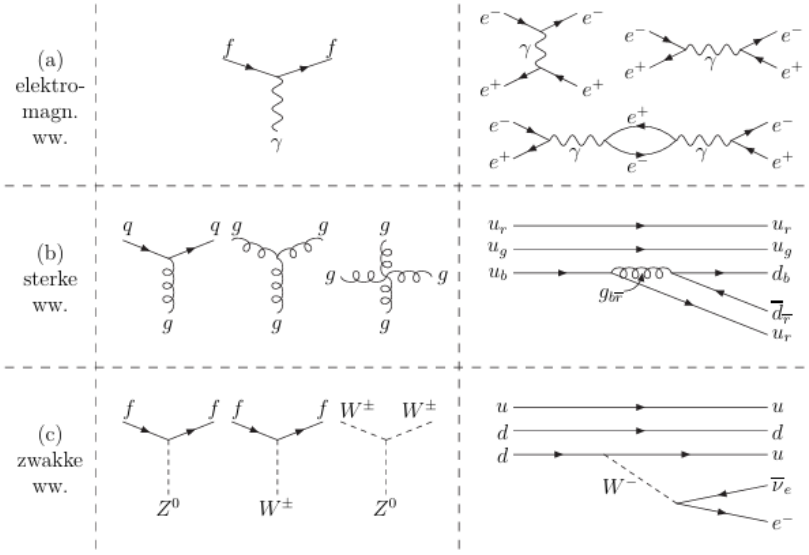

Figure 1.2: A selection of Feynman diagrams illustrating various fundamental interactions among particles, including electromagnetic, strong, and weak processes [6].

Figure 1.2 showcases various examples. In these diagrams, solid lines represent fermions (leptons and quarks), while the fundamental bosons are illustrated by different types of lines: wavy lines for photons, curly lines for gluons, and dashed lines for Z- and W-bosons. The direction of particle movement is typically from left to right. Arrows on the lines indicate the direction associated with a positive fermion number, with arrows on antiparticle lines pointing in the opposite direction. This convention is based on the interpretation of an antiparticle's wave function with negative energy as a particle's wave function with positive energy moving backward in time.

The Feynman rules, which we will apply later, offer a method to calculate scattering amplitudes using these diagrams. In simplified terms, a coupling factor is assigned to each vertex (interaction point), and propagator factors are applied to internal lines. For instance, in Quantum Electrodynamics (QED)—the

theory describing particle interactions via electromagnetic forces—the coupling constant is defined as [6],

$$\alpha = \frac{e^2}{4\pi\hbar c} \tag{1.2}$$

At each vertex, a factor of $\sqrt{\alpha}$ is included in the scattering amplitude calculation. This factor essentially represents the probability of particles scattering or interacting during a collision. To construct diagrams for collisions involving electromagnetic interactions, one starts with a basic diagram like the one shown in Figure 1.2a. Because only incoming and outgoing particles are directly observable, numerous diagrams might represent the same physical process. Figure 1.2a depicts some of these possibilities for electron-positron scattering. The total scattering amplitude is the sum of these individual amplitudes. Given that the coupling constant α diagrams featuring many vertices contribute insignificantly. The probability of a transition is determined by squaring the total amplitude, which can be expressed as a series expansion in α. Terms of higher order in this series correspond to the Born expansion of the scattering probability [6].

These theoretical frameworks lead us to the experimental domain of particle physics, where data is gathered through recreating these collisions at CERN in Switzerland.

1.3 CERN's Particle Accelerators

Having covered the foundational concepts of particle physics, let's delve into the experimental discovery of these particles and the pivotal role of CERN in this scientific endeavor. CERN's main goal is to probe the universe's composition, understand its workings, and uncover its origins. This is accomplished by accelerating particles to speeds approaching 99.999999% of the speed of light, using sophisticated particle accelerators. Within such high-speed collisions, for example between protons, the quarks inside interact via the fundamental forces, generating new particles in the process. The detection and identification of these particles, along with the discovery of new ones, are key steps in answering the profound questions CERN seeks to address. A notable milestone was the identification of the Higgs Boson in 2012 [**?**], a discovery made through the data from colliding protons.

Figure 1.3 provides a glimpse into the assortment of particle accelerators at CERN, along with the various experiments and detectors in use. The journey of a particle bundle set for collision starts at the Proton Synchrotron (PS), where it undergoes initial acceleration up to 26 GeV [1]. From there, it moves to the Super Proton Synchrotron (SPS), which can boost it up to 450 GeV. This bundle is eventually split into two, with each half being sent in opposite directions within the Large Hadron Collider (LHC) to collide [7].

The Large Hadron Collider (LHC) stands as the world's most potent and largest particle accelerator. Encompassing a 27-kilometer circular tunnel buried underground, the LHC is equipped with four major detectors placed around the tunnel to capture the outcomes of particle collisions, which are,

- **ATLAS (A Toroidal LHC ApparatuS):** A versatile detector designed for a broad range of physics investigations, including the search for the Higgs boson and the exploration of fundamental forces and particles [7].
- **CMS (Compact Muon Solenoid):** Another general-purpose detector with a specific emphasis on precise measurements of particles, particularly focusing on the properties of muons. CMS played a vital role in the discovery of the Higgs boson [7].

[1] With the relativistic kinetic energy given by $E_{\text{kin}} = \frac{mc^2}{\sqrt{1-\frac{v^2}{c^2}}} - mc^2$, we can find the speed of the particle.

- **ALICE (A Large Ion Collider Experiment):** Specialized in the study of heavy-ion collisions, ALICE contributes to our understanding of quark-gluon plasma, a state of matter believed to have existed in the early universe [7].
- **LHCb (Large Hadron Collider beauty):** With a primary focus on investigating the asymmetry between matter and antimatter, LHCb examines the properties of particles containing the beauty (b) quark [7].

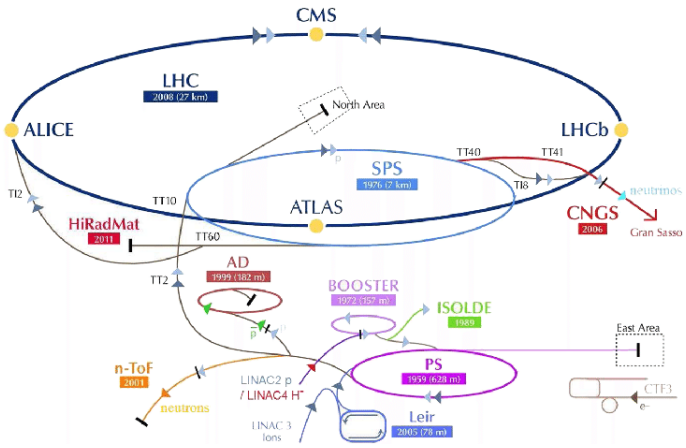

Figure 1.3: Detailed schematic of the CERN particle physics laboratory, showing major experiments and accelerators such as the Large Hadron Collider (LHC), ATLAS, CMS, and other facilities [9].

The focus of this study is specifically on the Drell-Yan process at a collision energy of 13 TeV, which we will explore in detail in the forthcoming chapters. The Drell-Yan process is characterized by the annihilation of a quark and an antiquark, leading to the creation of either a virtual photon or a Z boson. This intermediate boson then decays into a lepton and its corresponding antilepton. The electroweak interaction, a theory that merges the electromagnetic and weak nuclear forces, plays a crucial role in mediating this process. However, the initial quark-antiquark annihilation falls under the domain of the strong force, necessitating the application of quantum chromodynamics (QCD) to fully describe the interaction [8, p.301].

1.4 Strong Nuclear Force

The strong nuclear force, also known as the strong interaction, is a fundamental force of nature that binds quarks and gluons together to form protons, neutrons, and other hadrons. This force operates over a very short range, limited to the dimensions of atomic nuclei, and is powerful enough to overcome the electrostatic repulsion between positively charged protons within nuclei. Gluons, the exchange particles of the strong force, mediate this interaction.

A unique feature of the strong force is that it intensifies as quarks approach each other, a property known as confinement. This ensures quarks are always found in groups, forming color-neutral particles, rather than existing in isolation [10].

Color charge, a concept exclusive to the strong force, describes the quantum property of quarks and comes in three varieties: red, green, and blue, with corresponding anti-colors for antiquarks (anti-red, anti-green, and anti-blue). The formation of particles requires that quarks combine to create a color-

neutral entity, analogous to how mixing red, green, and blue light yields white light.

Gluons differ from photons, the mediators of the electromagnetic force, in that gluons carry a color charge. This enables them to not only interact with quarks but also to exchange color charge among them. With the ability to bear combinations of color and anti-color, gluons can manifest in eight distinct color-anti-color pairings, facilitating a complex interplay of strong force interactions within hadrons [5].

Hadrons play a crucial role in our research, particularly in the Drell-Yan process, where these particles are collided with each other. Composed of quarks, hadrons are categorized into two primary types [5],

- **Baryons:** These hadrons are made of three quarks. Protons, with two up quarks and one down quark, and neutrons, composed of two down quarks and one up quark, are prime examples of baryons.
- **Mesons:** In contrast to baryons, mesons comprise a quark and an antiquark pair. Mesons are inherently unstable and typically have a much shorter lifespan than baryons.

The theoretical framework governing the strong force is known as Quantum Chromodynamics (QCD). QCD enables the prediction of various phenomena stemming from hadron collisions, such as those observed at the Large Hadron Collider (LHC). Nonetheless, modeling these interactions precisely is challenging due to the complex nature of particle interactions within hadrons, where straightforward perturbative QCD calculations are often not feasible. To analyze the Drell-Yan process, we rely on Quantum Chromodynamics (QCD) to offer a theoretical foundation. This thesis will focus on understanding how the Drell-Yan process varies with different lepton masses. We will systematically derive the required QCD expressions to support our analysis.

2 Quantum Chromodynamics

This chapter is mostly based on reference[13],[16].

The Drell-Yan process involves a high-energy collision between two hadrons, which are particles made of quarks bound by the strong force. These collisions happen at very high speeds, close to the speed of light, and produce many new particles, including pairs of leptons. Due to the high velocities and the tiny scale of the particles, we need to use both special relativity and quantum theory to understand these events.

Quantum field theory (QFT) is the framework that integrates quantum mechanics, special relativity, and classical field theory. Within this framework, Quantum Chromodynamics (QCD) specifically deals with the strong interaction. While these theories are crucial for comprehending phenomena like the Drell-Yan process, this thesis will aim to explain only the necessary concepts and derivations for our analysis, considering my limited expertise in quantum field theory [11].

Another important theory, Quantum Electrodynamics (QED), focuses on the electromagnetic interactions among electrons, positrons, and other charged particles, using principles from quantum mechanics and special relativity. The force carriers in QED are photons, unlike the gluons in QCD. QED is a gauge field theory based on the U(1) Lie group [5], which means,

- **A gauge theory** models the behavior of fields, which are mathematical constructs representing physical properties. These theories are characterized by local symmetry, meaning the equations describing the fields remain consistent under certain local changes .
- **A group** in mathematics is a collection of elements with an operation (like multiplication or addition) that combines any two elements to produce another element within the same group. The unitary group U(1) consists of all complex matrices that, when multiplied by their complex conjugate, yield the identity matrix. In QED, the U(1) symmetry ensures the theory's equations do not change under transformations related to electric charge conservation [12].

QED is simpler than QCD, mainly because it deals with only one type of charge, associated with the U(1) gauge group. This forms the basis of a gauge field theory. QCD, however, is based on the SU(3) gauge group, which accounts for the symmetry of color charge in three different 'colors'. The presence of three color charges in QCD, as opposed to the single electric charge in QED, significantly increases the theory's complexity [5].

Another key difference is in the group properties. U(1) is an abelian group, meaning its elements commute with each other. On the other hand, SU(3) is a non-abelian group, where the elements do not commute, adding further complexity to the theory. It's interesting to note the dimensionality of SU(3), which is 8-dimensional. This dimensionality aligns with the earlier discussion on the different quark-antiquark configurations a gluon can carry [5], [12].

With these distinctions in mind, we can view the gauge symmetry of the strong interaction in QCD as an extension of the principles found in QED. Therefore, throughout this study, we will navigate between both theories to deepen our understanding of Quantum Chromodynamics.

2.1 Quantum Chromodynamics: An Introductory Guide

Quantum Chromodynamics (QCD) is based on the existence of $N = 3$ colored spin-$\frac{1}{2}$ particles, known as quarks, across six different flavors. Corresponding to the SU(3) group, represented by 3×3 complex matrices,there are $N^2 - 1 = 8$ gauge bosons, or gluons, denoted by A^a_μ. Each gauge boson interacts uniquely with a specific type of charge, and these interactions are represented by matrices,

$$T^a; a = 1, ..., N^2 - 1 \tag{2.1}$$

These matrices obey specific commutation relations,

$$\left[T^a, T^b\right] = i f^{abc} T^c \tag{2.2}$$

In QCD, the structure constants f^{abc} are antisymmetric in all their indices. The charge quantum number in QCD, referred to as color, is represented by the matrices T^a. This establishes QCD as a theory with multiple vector particles (the eight gluons) and non-commuting charges, making it a non-abelian theory.

Similar to how the angular momentum (which is better known for physicist) operators J^i serve as generators of the rotation group, the matrices T^a are the generators of the color symmetry group in QCD. Quarks belong to what is called the fundamental representation, which has the dimensionality $n = N$ and is represented by ψ_i where $i = 1, 2, 3$ (or, in a more general SU(N) group, for $i = 1, 2, \ldots, N$). The generators in the matrix representation are provided by,

$$T^a \to \frac{1}{2}\lambda^a \tag{2.3}$$

where λ^a are the 8 Gell-Mann [14] 3×3 matrices,

$$\begin{aligned}
\lambda^1 &= \begin{bmatrix} 0 & 1 & 0 \\ 1 & 0 & 0 \\ 0 & 0 & 0 \end{bmatrix}, \quad \lambda^2 = \begin{bmatrix} 0 & -i & 0 \\ i & 0 & 0 \\ 0 & 0 & 0 \end{bmatrix}, \quad \lambda^3 = \begin{bmatrix} 1 & 0 & 0 \\ 0 & -1 & 0 \\ 0 & 0 & 0 \end{bmatrix}, \\
\lambda^4 &= \begin{bmatrix} 0 & 0 & 1 \\ 0 & 0 & 0 \\ 1 & 0 & 0 \end{bmatrix}, \quad \lambda^5 = \begin{bmatrix} 0 & 0 & -i \\ 0 & 0 & 0 \\ i & 0 & 0 \end{bmatrix}, \quad \lambda^6 = \begin{bmatrix} 0 & 0 & 0 \\ 0 & 0 & 1 \\ 0 & 1 & 0 \end{bmatrix}, \\
\lambda^7 &= \begin{bmatrix} 0 & 0 & 0 \\ 0 & 0 & -i \\ 0 & i & 0 \end{bmatrix}, \quad \lambda^8 = \frac{1}{\sqrt{3}} \begin{bmatrix} 1 & 0 & 0 \\ 0 & 1 & 0 \\ 0 & 0 & -2 \end{bmatrix}.
\end{aligned} \tag{2.4}$$

The adjoint representation in QCD has a dimensionality of $N^2 - 1$, where gluons are represented as A^a_μ with $a = 1, \ldots, 8$. The matrix representation of the generators in the adjoint representation is uniquely characterized by the structure constants,

$$(T^a) \to -i f^{abc} \tag{2.5}$$

For quark behavior analysis, we use the Dirac equation, a fundamental relativistic quantum wave equation. Initially described in QED for the spin-1/2 charged particles, this equation is given by,

$$\left(i\hbar\gamma^\mu \partial_\mu - mc\right)\psi = 0 \tag{2.6}$$

Where γ^μ are 4×4 gamma matrices or Dirac matrices with $\mu = 0, \ldots, 3$ ($\mu = 0$ is the time component),

$$\gamma^0 = \begin{bmatrix} I & 0 \\ 0 & -I \end{bmatrix} \tag{2.7}$$

$$\gamma^i = \begin{bmatrix} 0 & \sigma^i \\ -\sigma^i & 0 \end{bmatrix}, \quad i = 1,2,3 \tag{2.8}$$

In these formulas I is the 2x2 identity matrix , and σ^i denote the Pauli matrices. These gamma matrices are crucial for describing the behavior of relativistic fermions and maintain invariance under Lorentz transformations. The term ∂_μ signifies the spacetime derivative, where $\mu = 0,\ldots,3$.

In the context of the Dirac equation, ψ is not merely a complex wave function but a 4-component vector, or bispinor , which consists of two spinors [15], [1]

$$\psi = \begin{bmatrix} \psi_1 \\ \psi_2 \\ \psi_3 \\ \psi_4 \end{bmatrix} \tag{2.9}$$

This leads to the division of ψ into two parts,

$$\psi_A = \begin{bmatrix} \psi_1 \\ \psi_2 \end{bmatrix} \tag{2.10}$$

$$\psi_B = \begin{bmatrix} \psi_3 \\ \psi_4 \end{bmatrix} \tag{2.11}$$

A spinor is represented by two complex numbers, indicating that ψ in the Dirac equation is composed of four complex numbers at each spacetime point. The components ψ_1 and ψ_2 correspond to the states of spin-up and spin-down electrons, respectively, whereas ψ_3 and ψ_4 represent spin-up and spin-down positrons. This structure integrates both matter (electron, ψ_A) and antimatter (positron, ψ_B) components within each bispinor. For our purposes, it's sufficient to recognize ψ as a bispinor made up of complex numbers, without further exploration into the visualization of spinors [15].

In QED, the electron-photon interaction is described by modifying the derivative ∂_μ to include the interaction term, as follows,

$$\partial_\mu \rightarrow D_\mu = \partial_\mu + ieA_\mu \tag{2.12}$$

Where e is the electric charge, and A_μ represents the photon field.

In QCD, the modification of ∂_μ to include the gluon interactions is not represented by a single term but rather a sum of terms corresponding to each of the gluons. Each term incorporates a color-charge matrix,

$$\partial_\mu \rightarrow D_\mu = \partial_\mu + ig_s A^a_\mu T^a \tag{2.13}$$

Here, g_s is the strong-interaction coupling constant, ∂^a_μ are the gluon fields and T^a are the color-charge matrices.

To connect the initial and final states in a scattering process, we employ the S-matrix, or scattering matrix. The construction of such a matrix utilizes the Feynman rules associated with a Feynman diagram [5]. For QED, these rules can be derived using perturbation theory. To extend these rules to QCD, we apply the same principles but incorporate the additional complexity of the color matrix.

2.1.1 Feynman Rules

We will analyze a scattering process $\phi_1 + \phi_2 \rightarrow \phi_3 + \phi_4$ within the framework of QED using time-dependent perturbation theory. Our goal is to express physical cross-sections in terms of invariant

[1] Note that using gamma matrices is a way to formulate the dirac equation to satisfy commutation rules. It is totally possible to use other means to describe the dirac equation and which means the way we interpert ψ can change too.

scattering matrix elements (derive these Feynman rules). Perturbation theory, as encapsulated in the Feynman rules, facilitates the computation of S-matrix elements.

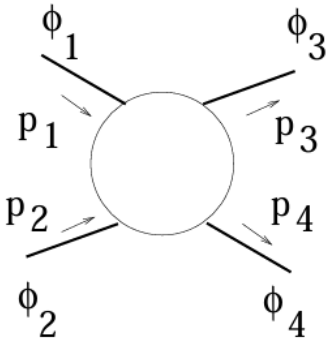

Figure 2.1: Feynman diagram illustrating a four-particle scattering process $\phi_1 + \phi_2 \to \phi_3 + \phi_4$ in QED. The diagram shows the exchange of momentum between the particles, represented by P_1, P_2, P_3, and P_4, as they interact via a central virtual particle [13].

Consider a relativistic, spin-1/2 system, incorporating the electromagnetic interaction into the Dirac equation as follows,

$$(i\partial\!\!\!/ - eA\!\!\!/ - m)\phi = 0 \tag{2.14}$$

Where $A\!\!\!/ = \gamma^\mu A_\mu$ (the same for $\partial\!\!\!/$). Here, the interaction potential is represented by,

$$V = -e\gamma^0\gamma^\mu A_\mu \tag{2.15}$$

Using first-order perturbation theory, we derive,

$$\begin{aligned}\mathscr{A} &= -i\int d^3x dt\, \phi_f^* V \phi_i \\ &= ie\int d^4x \bar{\phi}_f \gamma^\mu \phi_i A_\mu\end{aligned}$$

With ϕ_f the final state of the particles and ϕ_i the initial states of the particles. This leads to a $j\cdot A$ interaction form,

$$\mathscr{A} = -i\int d^4x\, j^\mu A_\mu \tag{2.16}$$

with the current j^μ defined as,

$$j^\mu = -e\bar{\phi}_f\gamma^\mu\phi_i \tag{2.17}$$

We express the initial and final states using plane-wave solutions,

$$\phi_k = N_k u(p_k) e^{-ip_k x} \tag{2.18}$$

where $N_k = \frac{1}{\sqrt{2E_kV}}$ for $k = 1,2,3,4$. Substituting these plane-wave solutions, we obtain,

$$\mathscr{A} = (2\pi)^4\delta^4(P_f - P_i)\Pi_f\left[\frac{1}{\sqrt{2E_fV}}\right]\Pi_i\left[\frac{1}{2E_iV}\right]\mathscr{M}_{fi} \tag{2.19}$$

Here, we encounter the scattering matrix element $\mathscr{M}_{fi}$ which is given by,

$$\mathscr{M}_{fi} = -e\bar{u}(p_3)\gamma_\mu u(p_1)\frac{-ig^{\mu\nu}}{q^2}e\bar{u}(p_4)\gamma_\nu u(p_2) \tag{2.20}$$

This formulation provides a precise representation of the scattering matrix elements, which are crucial for calculating the physical cross-sections of the scattering process being studied. The corresponding Feynman rule for the spin-1/2 transition vertex is then given by figure 2.2.

Figure 2.2: Feynman diagram illustrating the vertex interaction between an electron and a photon, symbolizing the fundamental electron-photon interaction in QED. This diagram depicts the electron (labeled by momentum p) emitting or absorbing a photon (μ), with the vertex factor represented by $ie\gamma^{\mu}$ [13].

In a manner similar to the electron-photon interaction in QED, we can derive the Feynman rule for the quark-quark-gluon coupling in QCD, which has a comparable structure but includes the complexities of color charges as seen in figure 2.3.

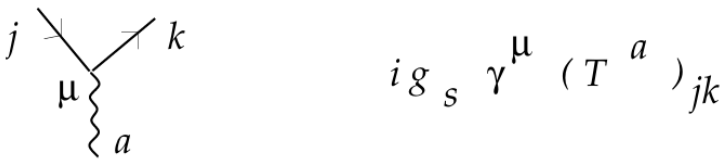

Figure 2.3: Feynman diagram for the quark-quark-gluon coupling in QCD. The gluon (labeled by μ, a) interacts with quarks (labeled by j, k), highlighting the color indices and the gluon's influence on quark dynamics within hadrons [13].

For internal particle lines, the Feynman rules for propagators are specified in figure 2.4.

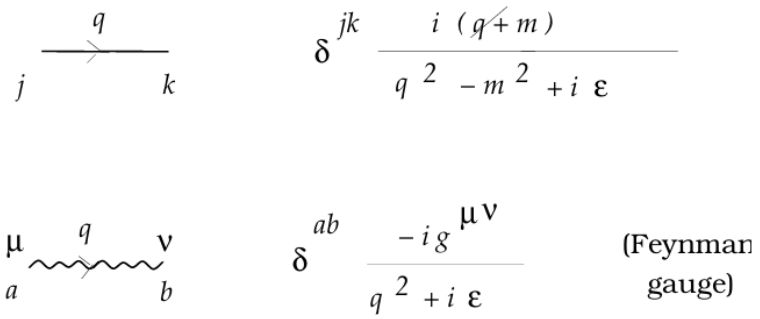

Figure 2.4: Feynman diagrams illustrating the propagators for quarks and gluons, fundamental components in quantum field calculations. The top diagram shows the quark propagator with momenta q and indices j and k, represented by the formula next to it. The bottom diagram presents the gluon propagator involving gluon fields μ and ν with color indices a and b, depicted by the expression next to it, highlighting the gauge-dependent nature of gluon interactions in QCD [13].

The quark-gluon interaction is not the sole interaction in QCD. Due to the nature of color charges in QCD and the presence of multiple vector particles, gluons, these particles are capable of self-interaction. This self-interaction is a result of how color charges behave uniquely within QCD. Unlike in electromagnetism, where the system remains unchanged under a specific transformation of the four-potential A_μ by a four-gradient,

$$A_\mu \to A_\mu + \partial_\mu \lambda \tag{2.21}$$

In QCD, the gauge freedom is extended to include not just a four-gradient modification but also a rotation in the color indices,

$$A^a_\mu \to A^a_\mu + \partial_\mu \lambda^a - g_s f^{abc} \lambda^b A^c_\mu \tag{2.22}$$

The non-zero structure constants f^{abc} modify the field strength tensor $F^{\mu\nu}$ in QCD compared to its QED counterpart. While in QED, it is defined as,

$$F_{\mu\nu} = \partial_\mu A_\nu - \partial_\nu A_\mu \tag{2.23}$$

In QCD, it includes an additional term,

$$F^a_{\mu\nu} = \partial_\mu A^a_\nu - \partial_\nu A^a_\mu + g_s f^{abc} A^b_\mu A^c_\nu \tag{2.24}$$

This extra term in $F^a_{\mu\nu}$ leads to gluon self-interactions in the construction of a gauge-invariant kinetic energy term for gluons by squaring $F^a_{\mu\nu}$. The squaring of $F^a_{\mu\nu}$ introduces both cubic and quartic gluon self-interaction terms. The cubic term, involving derivative couplings, is proportional to $g_s \times f$, and the quartic term, lacking derivatives, is proportional to $g_s^2 \times f^2$ and lacks derivatives.

The Feynman rules for these interactions are illustrated on figure 2.5.

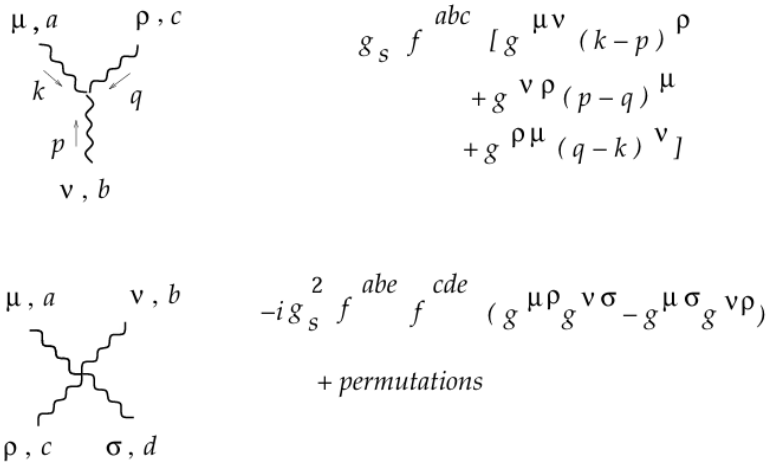

Figure 2.5: Feynman diagrams depicting gluon self-interactions and their coupling with quarks. The top diagram illustrates the three-gluon vertex with momentum and color labels, accompanied by the corresponding mathematical expression involving the structure constants f^{abc} and metric tensors $g^{\mu\nu}$. The bottom diagram shows the four-gluon vertex, highlighting the symmetrical nature of gluon interactions in non-abelian gauge theories like QCD with coefficients that ensure gauge invariance [13].

This structure ensures that the coupling constant g_s in the gauge boson self-interaction vertices matches the g_s in the quark-gluon interaction vertex, a crucial aspect for maintaining non-abelian gauge invariance.

2.2 Deep Inelastic Scattering

Having delved into foundational Quantum Chromodynamics (QCD) concepts, we now turn to Deep Inelastic Scattering (DIS), a pivotal experimental approach that reveals the internal composition of hadrons. Through DIS, where high-energy electrons scatter off quarks within hadrons, we gain access to structure functions. These functions are vital as they encode the distributions of quarks and gluons, thereby mapping the internal dynamics of hadrons. The structure functions will serve as foundational elements for the equations required to describe the Drell-Yan process.

Consinder directing a high-energy electron beam at a hadron and analyzing the scattering patterns, we can study the interactions between the electrons and the quarks inside the hadrons. This process is mediated by the exchange of virtual photons, which, unlike real photons, do not satisfy the mass shell condition $q^2 = 0$ or in simpler terms, the four-momentum is not conserved, allowing them to reveal details about the internal structure of the target particles.

The invariant mass W of the outgoing system is determined by the equation,

$$W^2 = (p_N + q)^2 = M_N^2 + 2p_N \cdot q + q^2 \tag{2.25}$$

Where M_N and p_N are the mass and four-momentum of the nucleus. It follows that q^2 is negative, thus we define $Q^2 \equiv -q^2$.

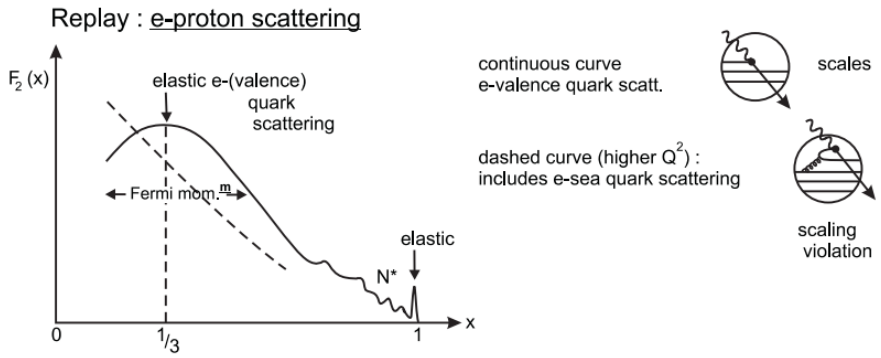

Figure 2.6: Schematic representation of electron-proton scattering, showing the structure function $F_2(x)$ as a function of Bjorken x (represents the momentum fraction of a parton). The graph delineates different scattering regimes, the elastic scattering at $x = 1$, and the inelastic scattering showing both valence and sea quark contributions. The continuous curve represents valence quark scattering, while the dashed curve at higher Q^2 includes sea quark scattering, illustrating scaling violations due to QCD effects [16].

Instead of delving into the detailed derivation, let's summarize and discuss the results of the experiment that guide us to the next part of our discussion. As Q^2 increases, we initially observe 'nuclear' scaling with a peak at $x_N = 1$ (situation where probing photon interacts with a single constituent quark or gluon), which then transitions to violations of this scaling (deviates from the expected value). Subsequently, 'proton' scaling emerges with a peak at $x \sim 1/3$. If quarks had substructures, further increases in Q^2 would lead to another cycle of scaling violations followed by a new scaling regime. However, historical data does not support this repetitive pattern. Instead, scaling violations are observed, but these are attributed to the quantum field theory of quarks and gluons (QCD) with the coupling constant α_s (which we will be seeing more of it in depth later on). The probing photon reveals the proton as being composed

of three valence quarks and an indefinite number of $q\bar{q}$ pairs from the sea quarks, which arise from gluons ($g \to q\bar{q}$. This dynamic is illustrated in figure 2.6. When the photon probes a quark carrying a fraction ξ of the proton's momentum p, and assuming the quarks are nearly massless, we find,

$$(\xi p + q)^2 = m_q^2 \approx 0 \tag{2.26}$$

leading to

$$\xi \approx \frac{Q^2}{2p \cdot q} = x \tag{2.27}$$

Therefore, as Q^2 increases, more partons (quarks and gluons) become visible, each holding a smaller fraction $\xi = x$ of the proton's momentum. This results in QCD scaling violations, depicted by the dashed line in figure 2.6, where the distribution of partons' momentum within the proton changes with Q^2.

2.2.1 The Structure Functions

Let's delve into a specific process: the Deep Inelastic Scattering (DIS) process $ep \to eX$, depicted in figure 2.7(a). We discuss the neutral current (NC) DIS mediated by γ and Z exchange, as well as the charged-current (CC) DIS mediated by W exchange, as shown in the second diagram (c).

Here, 'deep' implies $Q^2 >> M^2$ (mass of the proton), and 'inelastic' implies $W^2 = (p+q)^2 >> M^2$. The NC cross-section takes the form,

$$\frac{d\sigma}{dxdy} = xs\frac{d\sigma}{dxdQ^2} = \frac{2\pi y\alpha\hbar^2}{Q^4}\sum_j \eta_j L_j^{\mu\nu} W_{\mu\nu}^j \tag{2.28}$$

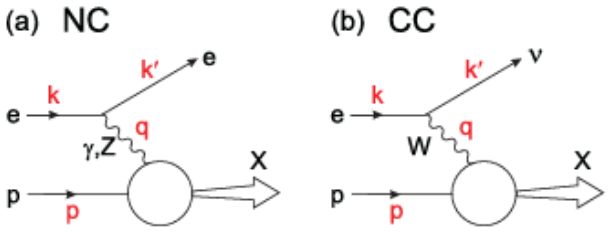

Figure 2.7: Illustration of Deep Inelastic Scattering (DIS) processes. (a) Neutral Current (NC) DIS mediated by photon (γ) and Z boson exchange, involving an electron scattering off a quark. (b) Charged Current (CC) DIS mediated by W boson exchange, where an electron is converted into a neutrino [16].

$L^{\mu\nu}$ is the tensor from the leptonic vertex known in terms of k (four-momentum of the incoming electron) and k' (four-momentum of the outgoing electron), and $W_{\mu\nu}$ is the unknown tensor describing the hadronic vertex. Although $W_{\mu\nu}$ is unknown, it must be constructed from the 4-momenta p, q, and the metric tensor $g_{\mu\nu}$. For unpolarized DIS, there are three tensor forms satisfying the requirements of current conservation $q^\mu W_{\mu\nu} = q^\nu W_{\mu\nu} = 0$. In this case, the general form is,

$$W_{\mu\nu} = \left(-g_{\mu\nu} + \frac{q_\mu q_\nu}{q^2}\right) F_1(x,Q^2) + \frac{\hat{P}_\mu \hat{P}_\nu}{p \cdot q} F_2(x,Q^2) - i\varepsilon_{\mu\nu\alpha\beta}\frac{q^\alpha p^\beta}{2p \cdot q} F_3(x,Q^2) \tag{2.29}$$

And here we find the observable structure functions that we were looking for! We can write a more general form of this equation by doing some algebraic manipulations,

$$\frac{d\sigma}{dxdQ^2} = \frac{2\pi\alpha^2}{xQ^4}\left[(Y_+F_2 \pm Y_- xF_3 - y^2F_L)\right] \tag{2.30}$$

where (with y the fraction of the lepton's energy lost in the nucleus frame),

$$Y_\pm = 1 \pm (1-y)^2 \quad \text{and} \quad F_L = F_2 - 2xF_1. \tag{2.31}$$

These functions, denoted by $F_i(x,Q^2)$, where $i = 1,2,3$ are functions of two scalar variables x and Q^2 which can be constructed from p and q. They provide information about how partons (quarks and gluons) are distributed within hadrons. In DIS, the cross section is expressed in terms of these structure functions, which encode information about the momentum distribution of quarks and gluons inside the proton. The reduced cross section, denoted by $\sigma_{\text{red}}(x,Q^2)$, is a combination of these structure functions and is often used in the analysis of experimental data. Let's expand the structure function to a more mathematical function that quantitavely describe the probablity density of finding a specific type of parton with a given momentum fraction x inside the hadron, called the parton distribution function.

2.2.2 The Quark Parton Model

The basic idea of the QPM is that in the DIS process, the virtual photon interacts with one of the quark constituents of the proton, see figure 2.8. We view the process from a frame in which the proton is moving very fast so that the relativistic time dillation slows down the rate with which the quarks interact with each other. Thus the struck quark appears essentially free during the short time that it interacts with the photon. As a result, the ep interaction may be written as an incoherent sum (of probabilities) of scattering from single free quarks,

$$\frac{d\sigma}{dxdQ^2} = \sum_q \int_0^1 d\xi f_q(\xi)\left(\frac{d\hat{\sigma}_{eq}}{dxdQ^2}\right) \tag{2.32}$$

where $f_q(\xi)$ is the probability of finding the quark q in the proton carrying a fraction ξ of its momentum.

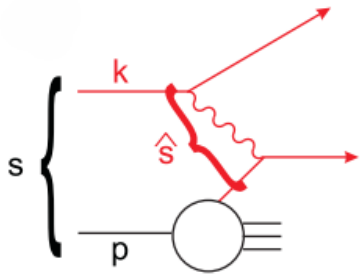

Figure 2.8: Diagram showing the interaction of an electron with a quark within a proton, emphasizing the quark's momentum transfer (ξ) during the collision [16].

The QPM formula can be written as,

$$\frac{d\sigma}{dxdQ^2} = \frac{2\pi\alpha^2}{Q^4}\sum_q \int_0^1 d\xi\, f_q(\xi)\, e_q^2\left[1+(1-y)^2\right]\delta(x-\xi). \tag{2.33}$$

If we rewrite the QPM formula in the form,

$$\frac{d\sigma}{dxdQ^2} = \frac{2\pi\alpha^2}{xQ^4}\sum_q \int_0^1 d\xi\, f_q(\xi)\, e_q^2 x'\delta(x-\xi), \tag{2.34}$$

and compare it with the general structure function formula, we obtain,

$$F_2 = 2xF_1 = \sum_q \int_0^1 d\xi\, f_q(\xi)\, x' e_q^2 \delta(x-\xi) = \sum_q e_q^2 x f_q(x). \tag{2.35}$$

The first equality, known as the Callan-Gross relation, holds because quarks have spin $\frac{1}{2}$. If the quarks had spin 0, then F_1 would have been 0. Note that in the QPM, the structure functions are independent of Q^2, exhibiting scaling behavior. The collective distribution of quarks and gluons are called, parton distribution functions (PDFs), denoted as $f_a(x)$, describe the probability of finding a quark or gluon carrying a fraction x of the proton's momentum when probed at a certain energy scale Q, like we explained earlier.

2.2.3 QCD Analysis of DIS Structure Functions

The structure function $F_2(x,Q^2)$ is analyzed in this section through a factorization formula that integrates QCD corrections to address the complex dynamics of parton interactions at higher energy scales (this is the range that interests us). High-energy (short-distance) interactions are treated using perturbative methods, exploiting the property of asymptotic freedom in QCD where the coupling constant becomes weaker at high energies (this will be coming back later). This allows for precise calculations of the scattering processes involving quarks and gluons. On the other hand, low-energy (long-distance) interactions are inherently non-perturbative and thus more challenging to compute. These interactions often involve the binding dynamics of quarks and gluons within the proton, encapsulated by Parton Distribution Functions (PDFs). Factorization in DIS effectively separates the perturbative components from the non-perturbative elements, enabling a clear analysis of hard scattering processes. This separation is essential, particularly in high-energy collisions, where we examine interactions at scales where partons behave almost freely due to the high momentum transfer.

The comprehensive collinear factorization formula for the structure function F_2 is given by [8],

$$\begin{aligned} F_2(x,Q^2) =& x\sum_{q,\bar{q}} e_q^2 \int_x^1 \frac{d\xi}{\xi} g(\xi,Q^2)\left\{\delta\left(1-\frac{x}{\xi}\right) + \frac{\alpha_s}{2\pi} C_g^{\overline{\text{MS}}}\left(\frac{x}{\xi}\right) + \dots\right\} \\ &+ x\sum_{q,\bar{q}} e_q^2 \int_x^1 \frac{d\xi}{\xi} g(\xi,Q^2)\left\{\frac{\alpha_s}{2\pi} C_g^{\overline{\text{MS}}}\left(\frac{x}{\xi}\right) + \dots\right\}. \end{aligned} \tag{2.36}$$

In this formula,

- x represents the Bjorken scaling variable, indicating the fraction of the proton's momentum carried by the struck parton.
- Q^2 is the momentum transfer in the interaction, serving as the scale at which the structure is probed.
- The sum $\sum_{q,\bar{q}}$ denote summations over quark and antiquark flavors.
- e_q is the electric charge of the quark flavor q.
- $g(\xi,Q^2)$ is the parton distribution function, describing the probability of finding a parton with a momentum fraction ξ at the scale Q^2.

- The delta function $\delta(1-\frac{x}{\xi})$ represents the leading-order contribution.

- $\frac{\alpha_s}{2\pi}C_g^{\overline{\text{MS}}}(\frac{x}{\xi})$ reflects higher-order corrections in the Modified Minimal Subtraction scheme ($\overline{\text{MS}}$) [2]. The $\overline{\text{MS}}$ scheme regularization method used in quantum field theory that simplifies calculations by subtracting only the divergent parts of loop integrals, along with a specific set of finite terms defined by the dimensional regularization technique.

This extended formulation allows for a more accurate prediction and analysis of the structure function across different kinematic ranges.

Later, we will explore how the structure function F_2, obtained from Deep Inelastic Scattering (DIS) experiments, measures the probability of finding a parton carrying a fraction x of the proton's momentum at a specific momentum transfer scale Q^2. Due to its dependence on Q^2, we can use this experimentally derived information to calculate the behavior of partons inside a hadron. This calculation involves an evolution equation that we will derive later.

Let's summarize our progress so far: We began with a brief introduction to Quantum Chromodynamics (QCD) and proceeded to discuss a specific experimental framework, Deep Inelastic Scattering (DIS). In the context of DIS, we explored structure functions and subsequently derived Parton Distribution Functions (PDFs). This framework allows us to describe the internal structure of hadrons quantitatively. However, our current understanding does not extend to detailed interactions and evolution of these internal structures through time. The next steps will exaclty involve deriving these evolution equation, but first, it is imperative to grasp some foundational concepts such as renormalization and the running of the QCD coupling constant, which has been alluded to previously.

2.3 Renormalization

Up to this point, our discussion has centered on tree-level effects, specifically considering Feynman diagrams without loop contributions. However, loop corrections become relevant at higher orders in perturbation theory. Such corrections to the processes introduce new complexities that require a systematic approach to address.

In the following sections, we will explore loop effects. The theoretical framework that encompasses these effects is known as renormalization. We aim to provide an introductory overview of renormalization and its physical interpretations, which we will further clarify with an example involving the renormalization of the electric charge.

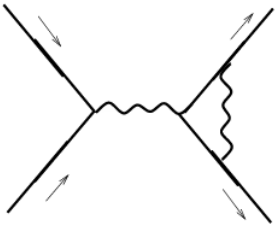

Figure 2.9: Feynman diagram depicting loop corrections in a particle interaction. This diagram illustrates the inclusion of higher order effects in perturbation theory [13].

[2] Extra information about this scheme can be found in [17, p.3-4]

2.3.1 Basic Principles of Renormalization

A clear indication that renormalization is necessary emerges when evaluating Feynman diagrams with loops, which often result in integrals that are divergent in the ultraviolet (high-momentum) region. Renormalization gives meaning to these ultraviolet divergences. For a Feynman graph with a loop integral of the form,

$$\int d^4k \frac{N(k)}{D(k)} \tag{2.37}$$

we assess the degree of divergence by examining the powers of the momentum k,

$$D = (\text{powers of } k \text{ in } N+4) - (\text{powers of } k \text{ in } D) \tag{2.38}$$

If $D \geq 0$, the integral is ultraviolet divergent. A theory is termed 'renormalizable' if it contains only a finite number of such divergent amplitudes. QED, for instance, has three divergent amplitudes. QCD, while more complex, still possesses only a finite number. In renormalizable theories, all divergent Feynman graphs include these few fundamental divergent amplitudes as their components.

Renormalizability ensures that we can systematically address the ultraviolet divergences. By adjusting the magnitudes of certain parameters and the properties of particles within the theory, these divergences can be absorbed. For a given quantity, which we will denote as ϕ, the renormalization scaling is applied as follows,

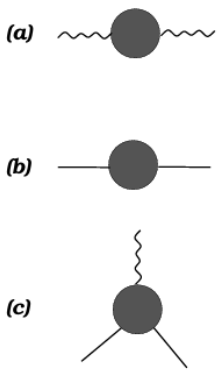

Figure 2.10: Examples of fundamental divergent Feynman diagrams. renormalization. (a) shows a loop with a single external momentum, illustrating a typical ultraviolet divergence. (b) and (c) depict self-energy and vertex correction diagrams, respectively, each fundamental to the renormalization process in theories like QED and QCD, where adjustments of parameters absorb these divergences [13].

$$\phi \rightarrow \phi_0 = Z\phi \tag{2.39}$$

Here, ϕ_0 represents the renormalized quantity, ϕ is the original quantity, and Z is a renormalization constant that compensates for the divergence. Although Z may itself be divergent or unobservable, when the adjustments are made and the predictions of the theory are expressed in terms of renormalized quantities, all physical observables are rendered finite and free from divergence.

This results in a description of the renormalization process, which we can outline as a series of steps:

- Use a method to deal with the troublesome divergences. Examples include setting a cut-off limit (Λ) on the ultraviolet region or using dimensional regularization.

- To get rid of the divergences, make specific changes to parameters and wave functions. In the case of QED, this involves tweaking the electromagnetic potential (A), the electron wave function (ψ) and mass (m), and the coupling constant (e). The adjustments look like this,

$$A \to A_0 = \sqrt{Z_3} A \tag{2.40}$$

$$\psi \to \psi_0 = \sqrt{Z_2}\psi \tag{2.41}$$

$$m \to m_0 = \frac{Z_m}{Z_2} m \tag{2.42}$$

$$e \to e_0 = \frac{Z_1}{Z_2\sqrt{Z_3}} e \tag{2.43}$$

  Here, Z_3 and Z_2 are constants for the photon and electron wave function, Z_1 is the vertex constant, and Z_m is the electron mass constant.

- After these adjustments, all the physical predictions become calculable and clearly defined in terms of these adjusted quantities, with no more divergences.

Theories that successfully yield finite predictions for physical quantities through this program are called renormalizable theories!

Before going to a specific example, we can point out that gauge invariance adds significant constraints to renormalization, establishing relationships among the divergent amplitudes and, consequently, the renormalization constants. Let's take QED as an example. Gauge invariance implies the following relation between the electron-photon vertex Γ_μ dotted into the photon momentum q^μ and the electron propagators S,

$$q^\mu \Gamma_\mu = S^{-1}(p+q) - S^{-1}(p) \tag{2.44}$$

This equation, illustrated in the figure below, is referred to as the Ward identity and holds true to all orders.

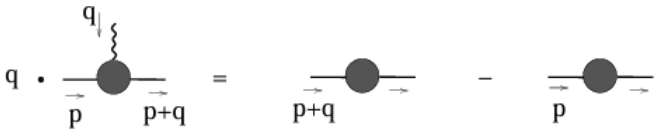

Figure 2.11: This diagram shows the application of the Ward identity, depicting how the photon's momentum q^μ interacts with the electron propagators. The equality demonstrates that gauge invariance maintains the conservation of current, crucial for ensuring physical observables are gauge-independent [13].

Using the renormalization constants Z_1 and Z_2 defined by the rescalings from earlier,

$$\Gamma^\mu = \frac{1}{Z_1}\gamma^\mu + \ldots \tag{2.45}$$

$$S(p) = \frac{Z_2}{\not{p} - m} + \ldots \tag{2.46}$$

we have

$$\frac{1}{Z_1}\not{q} = \frac{1}{Z_2}\left[(\not{p} + \not{q} - m) - (\not{p} - m)\right] \tag{2.47}$$

Thus in the abelian case (QED),

$$Z_1 = Z_2 \tag{2.48}$$

As a result, the rescaling relation defining the renormalized coupling in QED becomes,

$$e^2 = Z_3 e_0^2 \tag{2.49}$$

The renormalization of the electric charge is determined solely by the renormalization constant Z_3, which is associated with the photon wave function. This renormalization is independent of any factors related to the electron.

In contrast, in non-abelian gauge theories, the equivalence $Z_1 = Z_2$ found in QED does not hold. Nonetheless, the principles of non-abelian gauge invariance still enforce specific relationships between the renormalization constants. These relationships are more complex than in the abelian case, and we will explore examples of these in subsequent discussions. For now, we will focus on detailed calculations involving renormalization at the one-loop level.

2.3.2 Self-Energy in Gauge Bosons

Before delving into our example, we must consider the gauge boson self-energy, which is a fundamental aspect involving one of the divergent amplitudes as depicted in Figure 2.10. We can think of these amplitudes as the building blocks of our theory. Focusing on the one-loop contributions, the Feynman diagrams for the self-energy of the photon and gluon are illustrated in Figure 2.12. For the photon, the only contribution comes from the fermion loop graph, whereas for the gluon, additional diagrams involving gluon loops must be taken into account. These loops are essential for understanding the behavior of the gauge bosons within our framework.

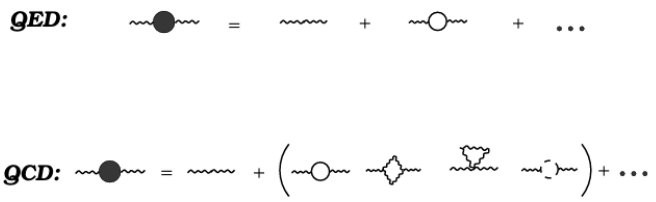

Figure 2.12: The top row (QED) shows the contributions to the photon self-energy, primarily from fermion loops. The bottom row (QCD) displays the gluon self-energy, including both fermion and additional gluon loop contributions, reflecting the non-abelian nature of QCD where gluons interact with each other [13].

Because of the relations 2.48 and 2.49, in the case of QED, calculating the gauge boson self-energy is sufficient to determine the renormalization of the coupling. The outcome of this section will be employed in the next section to explore the renormalized electric charge.

We now compute the fermion loop graph.

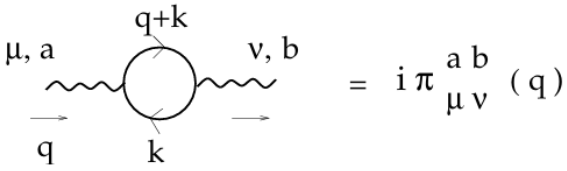

Figure 2.13: Diagram illustrating the fermion loop graph in QED. This graph shows a photon with momentum q interacting through a loop consisting of fermion-antifermion pairs, which significantly contributes to the photon's self-energy [13].

As shown in Figure 2.12, in the QED case the fermion loop is all that contributes to the self-energy, while in the QCD case this gives one of the required contributions. The graph in Figure 2.13 is given by,

$$i\pi^{ab}_{\mu\nu}(q) = -g^2 Tr\left(T^a T^b\right) \int \frac{d^4k}{(2\pi)^4} \frac{Tr\left[\gamma_\mu \left(\not{k}+\not{q}+m\right)\gamma_\nu \left(\not{k}+m\right)\right]}{\left(k^2-m^2+i0^+\right)\left((k+q)^2-m^2+i0^+\right)} \tag{2.50}$$

This expression is written for the non-abelian case in general. Here, the color-charge factor[3], is given by,

$$\mathrm{Tr}\left(T^a T^b\right) = \frac{1}{2}\delta^{ab} \tag{2.51}$$

To obtain the QED case, we make the following substitutions,

$$g^2 \to e^2 = 4\pi\alpha, \tag{2.52}$$

$$\mathrm{Tr}\left(T^a T^b\right) \to 1. \tag{2.53}$$

The integral in question is ultraviolet divergent. By performing superficial power counting in the loop momentum k, the divergence is identified as quadratic. However, gauge invariance necessitates that $\pi_{\mu\nu}$ be proportional to the transverse projector $g_{\mu\nu}q^2 - q_\mu q_\nu$, such that,

$$\pi_{\mu\nu} = \left(g_{\mu\nu}q^2 - q_\mu q_\nu\right)\Pi(q^2). \tag{2.54}$$

To manage the divergence, dimensional regularization is employed. This technique adjusts the number of dimensions in the integrals, mitigating the degree of divergence. It transforms a quadratic divergence into a logarithmic one by reducing the number of momentum powers by two. In this method, the integral is extended from 4 to $d = 4-2\varepsilon$ dimensions by introducing a dimensionful scaling parameter μ, so that,

$$g^2 \frac{d^4k}{(2\pi)^4} \to g^2\left(\mu^2\right)^\varepsilon \frac{d^{4-2\varepsilon}k}{(2\pi)^{4-2\varepsilon}} \tag{2.55}$$

In dimensional regularization, a logarithmic divergence such as d^4k/k^4 manifests as a pole at $\varepsilon = 0$ (or $d = 4$). Ultraviolet divergences in the integral are indicated by poles in $1/\varepsilon$. The result for $\pi_{\mu\nu}$ in dimensional regularization becomes,

$$\begin{aligned}\pi^{ab}_{\mu\nu}(q) &= -\left(g_{\mu\nu}q^2 - q_\mu q_\nu\right)\mathrm{Tr}(T^a T^b)\frac{g^2}{4\pi^2}\Gamma(\varepsilon)\int_0^1 dx \left(\frac{4\pi\mu^2}{m^2 - x(1-x)q^2}\right)^\varepsilon 2x(1-x) \\ &\equiv \left(g_{\mu\nu}q^2 - q_\mu q_\nu\right)\Pi(q^2).\end{aligned} \tag{2.56}$$

The first factor on the right-hand side, consistent with gauge invariance, confirms that the self-energy of the gauge boson is purely transverse,

$$\left(g_{\mu\nu}q^2 - q_\mu q_\nu\right)q^\mu = 0, \quad \left(g_{\mu\nu}q^2 - q_\mu q_\nu\right)q^\nu = 0. \tag{2.57}$$

The transversality of the self-energy implies that loop corrections do not endow gauge bosons with mass in QED and QCD. The term $\mathrm{Tr}\left(T^a T^b\right)$ signifies the non-abelian charge factor, which reduces to 1 in the QED case. Next, $\frac{g^2}{4\pi^2}$ is the coupling constant, turning into $\frac{e^2}{4\pi^2} = \frac{\alpha}{\pi}$ for QED. The Euler gamma function $\Gamma(\varepsilon)$ encloses the logarithmic divergence, represented by the pole at $\varepsilon = 0$ in dimensional regularization,

$$\Gamma(\varepsilon) = \frac{1}{\varepsilon} - \gamma + \mathscr{O}(\varepsilon), \tag{2.58}$$

[3]This follows from color-algebra in QCD; the detailed derivation steps are not necessary for this thesis

where γ is the Euler-Mascheroni constant, approximately 0.5772. The first term in the integrand stems from the regularization process, reliant on the ratio between the regularization scale μ^2 and the combination of the mass scales m^2 and q^2. The last term, $2x(1-x)$, results from the specific Feynman diagram computation.

Isolating the ultraviolet divergent part of the self-energy at $q^2 = 0$, the higher q^2 powers in $\Pi(q^2)$ are finite. The simplified expression is,

$$\Pi(0) = -\mathrm{Tr}(T^a T^b)\frac{g^2}{4\pi^2}\Gamma(\varepsilon)\int_0^1 dx \left(\frac{4\pi\mu^2}{m^2}\right)^{\varepsilon} 2x(1-x)$$

$$\approx -\mathrm{Tr}\left(T^a T^b\right)\frac{g^2}{12\pi^2}\frac{1}{\varepsilon} + \ldots \tag{2.59}$$

For the QED case specifically, the approximation yields,

$$\Pi(0) \approx -\frac{\alpha}{3\pi}\frac{1}{\varepsilon} + \ldots \tag{2.60}$$

Armed with these results, we will proceed to discuss the renormalization of the electromagnetic coupling in our forthcoming example.

2.3.3 Renormalization of The Electromagnetic Coupling

Consider a physical process involving the exchange of photons. The effect of renormalization on the photon propagator can be understood by considering multiple photon self-energy insertions, depicted schematically in figure 2.14.

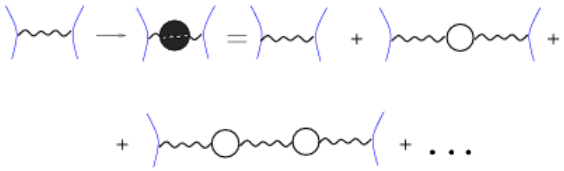

Figure 2.14: Schematic representation of the renormalization effects on the photon propagator due to repeated self-energy insertions. This sequence shows how the bare photon propagator D_0 is modified through successive insertions of the self-energy Π, illustrating the series expansion used in the renormalization process in QED [13].

$$D_0 \to D = D_0 + D_0\Pi D_0 + D_0\Pi D_0\Pi D_0 + \ldots \tag{2.61}$$

Where D_0 is the bare photon propagator, and Π represents the photon self-energy computed in equation 2.60. By summing this series and applying the transverse projector in Π, along with the fact that longitudinal contributions vanish due to gauge invariance, we obtain,

$$D_0 \to D = \frac{D_0}{1-\Pi(q^2)}. \tag{2.62}$$

Consequently, the effect of renormalization on the photon exchange process can be described as,

$$\frac{e_0^2}{q^2} \to \frac{e_0^2}{q^2}\frac{1}{1-\Pi(q^2)}, \tag{2.63}$$

where q is the photon's momentum.

Separating the divergent and finite parts of Π, we can express the denominator on the right-hand side as,

$$1-\Pi(q^2) = [1-\Pi(0)]\left[1-\left(\Pi(q^2)-\Pi(0)\right)\right] + \mathcal{O}(\alpha^2). \tag{2.64}$$

Thus, we find,

$$\frac{e_0^2}{q^2} \to \frac{e_0^2}{q^2}\frac{1}{1-\Pi(q^2)} \tag{2.65}$$

$$\approx \frac{1}{q^2}\frac{e_0^2}{1-\Pi(0)}\frac{1}{1-[\Pi(q^2)-\Pi(0)]}. \tag{2.66}$$

From this expression, we identify two main effects of renormalization:

1. The coupling strength is modified to,

$$\frac{e_0^2}{1-\Pi(0)} \equiv e^2. \tag{2.67}$$

Comparing with equation 2.49, we find the renormalization constant Z_3,

$$Z_3 \approx 1+\Pi(0) \tag{2.68}$$

$$= 1-\frac{\alpha}{3\pi}\frac{1}{\varepsilon}+\dots \tag{2.69}$$

where we have utilized the explicit result for $\Pi(0)$. The coupling e represents the physical, renormalized coupling derived from the bare coupling e_0 via a divergence-managing rescaling.

2. The coupling becomes dependent on the momentum transfer q^2, dictated by the finite part of the self-energy, $\Pi(q^2)-\Pi(0)$. This dependence is divergence-free and observable. The dependence of the electromagnetic coupling on q^2 introduces a novel physical effect due to loop corrections. For low q^2 (as $q^2 \to 0$),

$$\Pi(q^2)-\Pi(0) \to 0, \tag{2.70}$$

and for high q^2 ($q^2 \gg m^2$),

$$\Pi(q^2)-\Pi(0) \approx \frac{\alpha}{3\pi}\ln\frac{q^2}{m^2}. \tag{2.71}$$

Therefore, e^2 signifies the coupling value at $q^2=0$, and we observe an increase in the coupling strength as q^2 increases. Rewriting this in terms of the fine structure constant for large momenta gives,

$$\alpha(q^2) = \frac{\alpha}{1-\left(\frac{\alpha}{3\pi}\ln\frac{q^2}{m^2}\right)}. \tag{2.72}$$

This q^2-dependence of the coupling is known as the running coupling, a concept we will explore further.

The result for the electromagnetic coupling illustrates the sum of perturbative terms containing large logarithms when $q^2 \gg m^2$. Expanding the equation in powers of α, we get,

$$\alpha(q^2) = \alpha\left(1+\frac{\alpha}{3\pi}\ln\frac{q^2}{m^2}+\dots+\frac{\alpha^n}{(3\pi)^n}\ln^n\frac{q^2}{m^2}+\dots\right). \tag{2.73}$$

This analogy likens the result to assembling a puzzle from small pieces (α), noting that corrections can become significantly complex at higher levels. However, by expressing the outcome via an effective measure ($\alpha(q^2)$), the series simplifies and becomes more manageable.

2.4 Renormalization Group

Let's explore renormalization from the perspective of the renormalization group. In previous discussions, we noted that the introduction of renormalization introduces a dependence on the renormalization scale μ in loop calculations. Given that the choice of μ is arbitrary, the laws of physics should remain invariant regardless of the scale we choose. This concept is accurately captured by the renormalization group. By examining how the theory evolves with the renormalization scale μ, we can gain valuable insights into the behavior of the theory at extremely short distances.

2.4.1 Renormalization Scale and Evolution Equations

In this section, we're going to look at how we can understand the way some physical measurements depend on a scale we choose, the renormalization scale μ. This is important because it lets us study a specific physical quantity, let's call it G, in a way that makes sense across different scales. When we talk about 'renormalization', we're essentially finding a way to deal with infinite or undefined values that can pop up in our calculations. We do this by using something called a renormalization constant, denoted as Z, to adjust the original (or unrenormalized) version of G, which we'll call G_0. This process allows us to redefine G in a way that includes the effects of the chosen scale μ and a certain parameter that changes with the scale, known as the renormalized coupling. This can be written as,

$$G_0(p_i, \alpha_0) = ZG(p_i, \alpha, \mu) \tag{2.74}$$

Here, p_i represents the set of physical momenta on which G depends, α is the renormalized coupling, and α_0 is the unrenormalized coupling. Given that the left-hand side does not depend on μ,

$$\frac{d}{d\ln\mu^2} G_0 = 0 \tag{2.75}$$

it follows that

$$\frac{d}{d\ln\mu^2}(ZG) = 0 \rightarrow \frac{\partial G}{\partial \ln\mu^2} + \frac{\partial G}{\partial \alpha}\frac{\partial \alpha}{\partial \ln\mu^2} + \frac{\ln Z}{\partial \ln\mu^2} G = 0 \tag{2.76}$$

By defining

$$\beta(\alpha) = \frac{\partial \alpha}{\partial \ln\mu^2} \tag{2.77}$$

$$\gamma(\alpha) = \frac{\partial \ln Z}{\partial \ln\mu^2} \tag{2.78}$$

we can rewrite the equation as,

$$\left[\frac{\partial}{\partial \ln\mu^2} + \beta(\alpha)\frac{\partial}{\partial \alpha} + \gamma(\alpha)\right] G(p_i, \alpha, \mu) = 0 \tag{2.79}$$

where $\beta(\alpha)$ and $\gamma(\alpha)$ are calculable functions of α.

Now, suppose we measure G at a physical mass scale Q, which we use to rescale the arguments in G and set,

$$G(p_i, \alpha, \mu) = F(x_i, t, \alpha) \tag{2.80}$$

where

$$x_i = \frac{p_i}{Q} \tag{2.81}$$

$$t = \ln\frac{Q^2}{\mu^2} \tag{2.82}$$

The equation then becomes,

$$\left[-\frac{\partial}{\partial t}+\beta(\alpha)\frac{\partial}{\partial \alpha}+\gamma(\alpha)\right]F(t,\alpha)=0 \tag{2.83}$$

where from now on, we will not explicitly write the dependence on the rescaled physical momenta x_i in F.

Equation 2.83 represents the renormalization group evolution equation, which can be solved with the boundary condition $F(0,\alpha)$ at $t=0$, implying that $\mu = Q$. To solve this, we initially find the solution for the case when $\gamma = 0$ and then extend this solution to any value of γ. For the case where $\gamma = 0$, the equation simplifies to,

$$\left[-\frac{\partial}{\partial t}+\beta(\alpha)\frac{\partial}{\partial \alpha}\right]F(t,\alpha)=0 \tag{2.84}$$

Now, if we construct $\alpha(t)$ such that,

$$t=\int_{\alpha}^{\alpha(t)}\frac{d\alpha'}{\beta(\alpha')} \tag{2.85}$$

then any function F of the form,

$$F(t,\alpha)=F(0,\alpha(t)) \tag{2.86}$$

will satisfy the equation and the boundary condition. Here, t defines $\alpha(t)$ as an implicit function.

For the general case where $\gamma \neq 0$, the solution is derived from the $\gamma = 0$ solution by multiplying it with the exponential of an integral over γ, as follows,

$$F(t,\alpha)=F(0,\alpha(t))exp\left[\int_{\alpha}^{\alpha(t)}d\alpha'\frac{\gamma(\alpha')}{\beta(\alpha')}\right] \tag{2.87}$$

$$=F(0,\alpha(t))exp\left[\int_{0}^{t}dt'\gamma(\alpha(t'))\right] \tag{2.88}$$

In the second line, the variable of integration is changed using equation 2.85. This formula suggests that after we deal with the infinite values that pop up in our calculations through a process called renormalization, we can make our results accurate across different scales, from μ to Q, by doing two things:

1. We switch out α for a new version, $\alpha(t)$, which changes with time or scale. This is like updating our measurements to reflect how things change at different scales.

2. We apply a special adjustment based on a formula that includes γ, which tells us how to scale our results over time. This adjustment is kind of like a correction that takes into account how things stretch or shrink over different scales.

This correction changes how our results scale with t, adding new details that weren't there before, thanks to something called the anomalous dimension, γ. When we adjust our formula to include this, it helps us avoid problems with infinite values in our predictions and makes our expansion series more accurate. It does this by adding extra terms that become important at all levels of our calculations, helping us get more precise results without the issue of increasingly large corrections.

2.4.2 Renormalization Group Analysis of Photon Self-Energy

Let's revisit the study of photon self-energy, this time through the renormalization group perspective. The divergent part of the renormalization constant Z_3 helps us determine the QED β function at the

one-loop level.

The β function describes how the coupling strength α varies with the energy scale μ. This relationship is expressed as,

$$\alpha\left(\mu^2\right)^{\varepsilon} = Z_3\alpha_0 \tag{2.89}$$

By using expression 2.69 we have,

$$\frac{\partial\alpha}{\partial\ln\mu^2} = -\varepsilon\left(1-\frac{\alpha}{3\pi\varepsilon}\right)\alpha_0\left(\mu^2\right)^{-\varepsilon} = \frac{1}{3\pi}\alpha^2 \tag{2.90}$$

The leading term of the QED β function at small coupling is given by,

$$\beta(\alpha) = b\alpha^2 + \mathcal{O}(\alpha^3) \tag{2.91}$$

$$b = \frac{1}{3\pi} \tag{2.92}$$

We finally find after substituting this term,

$$\alpha(q^2) = \frac{\alpha}{1-b\alpha\ln(q^2/\mu^2)}, \quad b = \frac{1}{3\pi} \tag{2.93}$$

This equation reveals the leading term of the QED β function at low coupling strengths.

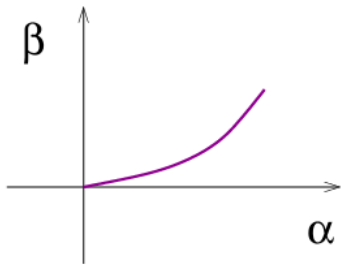

Figure 2.15: Graph depicting the leading term of the QED β function as a function of the coupling strength α. This curve highlights the relationship between the coupling constant and the rate of change of the coupling under renormalization group flow [13].

When we delve into how electric charge behaves at the microscopic level, we observe that its behavior becomes dependent on the energy involved. Initially, at a fundamental level, the charge appears to behave uniformly across all scales. However, when we factor in quantum corrections, we introduce a form of 'adjustment' factor, signified by an artificial or unphysical mass scale (such as μ).

Although this artificial scale vanishes in the final outcomes, a significant change persists: the behavior of the charge no longer remains constant across all energy levels. Instead, it varies depending on the specific energy scale under consideration. This entire process, with its adjustments and variations, is adeptly described by the renormalization group, which elucidates the universal trends in these adjustments through the β and γ functions. These functions are crucial for understanding and predicting how electric charge behaves as we explore the microscopic realm at different scales.

2.4.3 The β-function of QCD

Let's now finally explore the case of renormalization in QCD at the one-loop level, aiming to determine the one-loop β function, similar to our previous discussions.

We begin by rescaling the relations in QCD, which include the wave function and mass, as follows,

$$A \to A_0 = \sqrt{Z_3} A \tag{2.94}$$

$$\psi \to \psi_0 = \sqrt{Z_2}\psi \tag{2.95}$$

$$c \to c_0 = \sqrt{\tilde{Z}_3} c \tag{2.96}$$

$$m \to m_0 = \frac{Z_m}{Z_2} m \tag{2.97}$$

where, in addition to the renormalization constants of the abelian case, we also introduce $\tilde{Z}_3$. For renormalization of the coupling between quarks and gluons, we have,

$$Z_2\sqrt{Z_3} g_0 = Z_1 g \tag{2.98}$$

$$\tilde{Z}_3\sqrt{Z_3} g_0 \tag{2.99}$$

$$Z_3^{3/2} g_0 = Z_{1,3} g \tag{2.100}$$

$$Z_3^2 g_0^2 = Z_{1,4} g \tag{2.101}$$

We know that (without derivation) for non abelian guage invariance, that the vertices should have equal couplings. With this property we can find relations between the different Z as follows,

$$\frac{\tilde{Z}_1}{\tilde{Z}_3} = \frac{Z_1}{Z_2} = \frac{Z_{1,3}}{Z_3} = \sqrt{\frac{Z_{1,4}}{Z_3}} \tag{2.102}$$

In the non-abelian theory, we find that $Z_1 \neq Z_2$ (in QED they were equal).

Let's define the renormalized coupling from the quark-gluon vertex as follows,

$$\alpha_s \left(\mu^2\right)^{\varepsilon} = \frac{Z_2^2}{Z_1^2} Z_3 \alpha_{s,0} \tag{2.103}$$

Each of the renormalization constants Z_i can be expanded in a perturbation series, with the coefficients of this expansion being ultraviolet divergent. In dimensional regularization, these ultraviolet divergences manifest as poles at $\varepsilon = 0$, so the Z_i constants take the form,

$$Z_i = 1 + \alpha_s \frac{1}{\varepsilon} c_i + \text{finite term} \tag{2.104}$$

where the coefficients c_i correspond to the divergent terms and need to be calculated. Utilizing $\alpha_s \left(\mu^2\right)^{\varepsilon}$ and this expression, the β function is determined by,

$$\begin{aligned} \beta(\alpha_s) &= \frac{\partial \alpha_s}{\partial \ln \mu^2} \\ &= -\varepsilon \alpha_B (\mu^2)^{-\varepsilon} \left[1 - 2(Z_1 - 1) + 2(Z_2 - 1) + (Z_3 - 1)\right] \\ &= 2\alpha_s^2 (c_1 - c_2 - \frac{1}{2} c_3) \end{aligned} \tag{2.105}$$

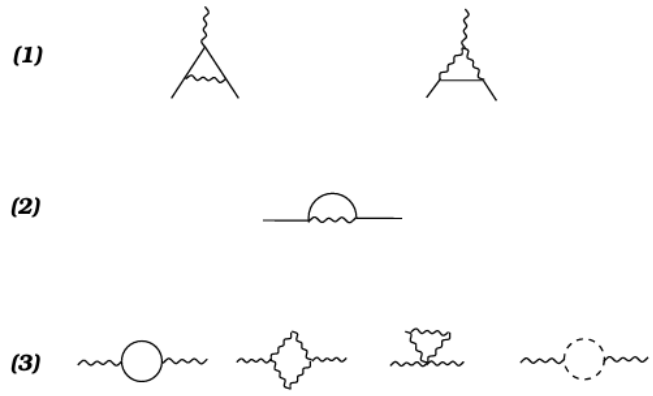

Figure 2.16: Illustration of one-loop Feynman diagrams contributing to the renormalization constants Z_1, Z_2, and Z_3 in QCD. Diagrams (1) show the quark-gluon vertex, (2) depict the quark self-energy, and (3) represent gluon self-energy and ghost contributions [13].

The Feynman diagrams that contribute to Z_1, Z_2, and Z_3 are the one-loop graphs for, respectively, the quark-gluon vertex, quark self-energy, and gluon self-energy renormalization. By calculating these diagrams using the method previously outlined for the fermion loop contributions and working in the Feynman gauge ($\xi = 1$), we derive the renormalization constants Z_i,

$$Z_1 = 1 - \frac{\alpha_s}{4\pi}\frac{1}{\varepsilon}(C_F + C_A) \tag{2.106}$$

$$Z_2 = 1 - \frac{\alpha_s}{4\pi}\frac{1}{\varepsilon}C_F \tag{2.107}$$

$$Z_3 = 1 + \frac{\alpha_s}{4\pi}\frac{1}{\varepsilon}\left(\frac{5}{3}C_A - \frac{4}{3}N_f T_F\right) \tag{2.108}$$

where N_f is the number of quark flavors, and the color charge factors are,

$$C_A = N = 3 \tag{2.109}$$

$$C_F = \frac{N^2-1}{2N} = \frac{4}{3} \tag{2.110}$$

$$T_F = \frac{1}{2} \tag{2.111}$$

Substituting these into the β function, we obtain,

$$\beta(\alpha_s) = 2\alpha_s^2(c_1 - c_2 - \frac{1}{2}c_3) = 2\frac{\alpha_s^2}{4\pi}\left(-C_F - C_A + C_F - \frac{1}{2}\frac{5}{3}C_A + \frac{1}{2}\frac{4}{3}N_f T_R\right)$$

$$= \frac{\alpha_s^2}{4\pi}\left(-\frac{11}{3}C_A + \frac{4}{3}N_f T_R\right) = -\frac{\alpha_s^2}{12\pi}(11N - 2N_f) \tag{2.112}$$

For $N_f < \frac{11N}{2}$, the β function in non-abelian theories like QCD becomes negative at small couplings, indicating asymptotic freedom,

$$\beta(\alpha_s) = -\beta_0\alpha_s^2 + \mathcal{O}(\alpha_s^3) \tag{2.113}$$

where

$$\beta_0 = \frac{1}{12\pi}(11N - 2N_f) \tag{2.114}$$

This behavior of the β function is opposite to the behavior of the β function in QED (equation 2.91)!

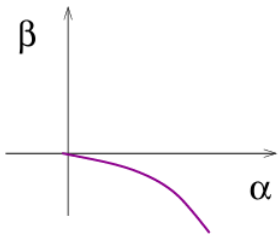

Figure 2.17: Graph displaying the behavior of the β function, contrasting with the behavior observed in QED as previously noted. This graph shows the β function decreasing with increasing coupling strength α [13].

This property of QCD, being weakly coupled at short distances, is critical for the perturbative calculation of scattering processes in the strong interaction at large momentum transfers. The renormalization group evolution equation incorporating this β function,

$$\frac{\partial \alpha_s}{\partial \ln \mu^2} = \beta(\alpha_s) \approx -\beta_0 \alpha_s^2 \tag{2.115}$$

and solving this,

$$\alpha_s(q^2) = \frac{\alpha_s(\mu^2)}{1 + \beta_0 \alpha_s(\mu^2) \ln \frac{q^2}{\mu^2}} \tag{2.116}$$

where β_0 was given already. We can see that QCD coupling decreases logarithmically as the momentum scale q^2 increases. This property is very important for perturbative calculation of scattering processes due to the strong interaction at large momentum transfers.

Let's summarize this part: In QCD, the running coupling constant α_s encapsulates the unique energy-dependent strength of the strong interaction, essential for understanding particle behavior across scales. Its decrease with increasing energy, known as asymptotic freedom, allows for perturbative calculations of processes like deep inelastic scattering, where partons interact within hadrons. This running coupling is integral to a specific evolution equation, which predict how parton distributions evolve with energy. Let's use everything we have learned until now to combine them in an equation.

3 Parton Branching Method: Collinear and TMD Distributions

This chapter is mostly based on reference[21].

3.1 Renormalization Group Evolution of Parton Distributions

Let's now write the renormalization group evolution equation of the parton distribution functions in terms of parton splitting processes (a parton emitting another parton) as follows,

$$\frac{\partial f_a(x,\mu^2)}{\partial \ln \mu^2} = \sum_b \int_x^1 \frac{dz}{z} P_{ab}(\alpha_s(\mu^2),z) f_b\left(\frac{x}{z},\mu^2\right) \tag{3.1}$$

where $f_a(x,\mu^2)$ are the parton distribution functions for $a = 1,\ldots,2N_f+1$ species of partons (with N_f the number of quark flavors) as functions of longitudinal momentum fraction x and evolution mass scale μ, and $P_{ab}(\alpha_s,z)$ are the DGLAP (Dokshitzer-Gribov-Lipatov-Altarelli-Parisi) splitting functions, depending on the running coupling α_s and the splitting variable z. These splitting functions represent the probability of a parton b to emit another parton and turn it into parton a, with z being the fraction of the original parton's momentum carried away by the emitted parton and we can write them as,

$$P_{ab}(\alpha_s,z) = \sum_{n=1}^{\infty} \left(\frac{\alpha_s}{2\pi}\right)^n P_{ab}^{(n-1)}(z) \tag{3.2}$$

We will work with the momentum-weighted parton distribution functions $\tilde{f}_a$,

$$\tilde{f}_a(x,\mu^2) = x f_a(x,\mu^2) \tag{3.3}$$

for which the evolution equations reads

$$\frac{\partial \tilde{f}_a(x,\mu^2)}{\partial \ln \mu^2} = \sum_b \int_x^1 dz P_{ab}(\alpha_s(\mu^2),z) \tilde{f}_b\left(\frac{x}{z},\mu^2\right) \tag{3.4}$$

Ofcourse, nothing is easy in QCD and this equation doesn't have a simple solution. The issue is that in the physical picture of the evolution equation, we're looking at how well we can distinguish between partons when they're packed closely together inside a proton or neutron and moving almost parallel to each other. There's a point beyond which we just can't tell them apart, determined by the energy at which we're observing them and the fundamental strength of the force that holds them together. If we ignore the tiny details that we can't see, it messes up our calculations, suggesting the sum of all possible outcomes doesn't add up as it should (unitarity gets broken). So, it's important to account for these tiny, blurred details to keep our predictions accurate.

To address this issue, we'll employ the 'Parton Branching Method'. This approach aims to maintain unitarity by reformulating the evolution equations with a focus on probabilities of no-branching (using Sudakov form factors) and probabilities of actual branching events. We plan to formally integrate the

resolution scale parameter z_M into the evolution equations.

To set up our formalism, we split the parton splitting functions into different components,

$$P_{ab}(\alpha_s,z) = \Delta_{ab}(\alpha_s)\delta(1-z) + K_{ab}(\alpha_s)\left[\frac{1}{1-z}\right]_+ + R_{ab}(\alpha_s,z) \tag{3.5}$$

where the plus-distribution $\left[\frac{1}{1-z}\right]_+$ (function used to manage integral that become infinite at certain points) is defined for any test function φ as,

$$\int_0^1 \frac{1}{(1-z)_+}\varphi(z)dz = \int_0^1 \frac{1}{1-z}[\varphi(z)-\varphi(1)]dz \tag{3.6}$$

Equation 3.5 organizes the singularities in the splitting functions $P_{ab}(\alpha_s,z)$ as $z \to 1$,breaking them down into a delta function $\delta(1-z)$ distribution, a plus distribution $\left[\frac{1}{1-z}\right]_+$, and the remainder function $R_{ab}(\alpha_s,z)$, that includes both logarithmic terms in $\ln(1-z)$ and regular terms as $z \to 1$. The $\delta(1-z)$ and $\left[\frac{1}{1-z}\right]_+$. The delta and plus-distributions are flavor diagonal (transitions or interaction can only occur between same types of quarks without chainging their flavour) and we can write them as,

$$D_{ab}(\alpha_s) = \delta_{ab}d_a(\alpha_s), \quad K_{ab}(\alpha_s) = \delta_{ab}K_a(\alpha_s) \tag{3.7}$$

The coefficients d_a and k_a, and the functions R_{ab} can be expanded as follows,

$$d_a(\alpha_s) = \sum_{n=1}^{\infty}\left(\frac{\alpha_s}{2\pi}\right)^n d_a^{(n-1)} \tag{3.8}$$

$$k_a(\alpha_s) = \sum_{n=1}^{\infty}\left(\frac{\alpha_s}{2\pi}\right)^n k_a^{(n-1)} \tag{3.9}$$

$$R_{ab}(\alpha_s,z) = \sum_{n=1}^{\infty}\left(\frac{\alpha_s}{2\pi}\right)^n R_{ab}^{(n-1)}(z) \tag{3.10}$$

Charge conjugation and SU(N_f) suggest that the rules governing how particles split into other particles, described by the splitting functions P_{ab} follow specific relations at all levels of calculation. Essentially, these symmetries ensure that the behavior of these splitting functions is predictable and consistent across different types of particles and interactions, no matter how complex the calculations become. These relations are,

$$P_{q_ig} = P_{\bar{q}_ig} = P_{qg}, \quad P_{gq_i} = P_{g\bar{q}_i} = P_{gq}$$

$$P_{q_iq_j} = P_{\bar{q}_i\bar{q}_j} = P_{qq}^{NS}\delta_{ij} + P_{qg'}^{S}, \quad P_{q_i\bar{q}_j} = P_{\bar{q}_iq_j} = P_{q\bar{q}}^{NS}\delta_{ij} + P_{q\bar{q}}^{S}$$

where the superscripts NS and S stand respectively for non-singlet and singlet. A non-singlet configuration involves particles that transform non-trivially under a symmetry operation, often maintaining distinct identities or flavors during interactions, this means they do not mix with particles of other flavors. On the other hand, a singlet configuration involves particles that transform into a combination that is invariant under symmetry operations, essentially appearing as a 'single' entity regardless of the symmetry applied. Consequently, the splitting functions, P_{ab} include three distinct interactions involving quarks and gluons or gluons with each other (P_{qg}, P_{gq}, and P_{gg}), alongside four distinct quark-quark interactions. These are divided into non-singlet components P_{qq}^{NS} and $P_{q\bar{q}}^{NS}$ and singlet components P_{qq}^{S} and $P_{q\bar{q}}^{S}$).

Let's try to find explicit expressions at one-loop and two-loop orders for the D_{ab}, K_{ab} and R_{ab} terms in equation 3.5.

3.2 Resolvable and Non-resolvable Emissions

We introduce a new important parameter, the soft-gluon resolution parameter z_M, into the evolution equations 3.4 by splitting the integration range on the right hand side into the resolvable ($z < z_M$) and non-resolvable ($z > z_M$) regions. In each region, we use the decomposition 3.5 in the evolution equations. We include terms through $O(1-z_M)$ but neglect power-suppressed contributions $O(1-z_M)^n, n \geq 2$.

Consider first the endpoint $z \to 1$ contribution from the K_{ab} term in the evolution equation 3.5. Using equation 3.6, we rewrite this as

$$\sum_b \int_x^1 dz \frac{K_{ab}(\alpha_s(\mu^2))}{(1-z)_+} \tilde{f}_b(x/z,\mu^2)$$

$$= \sum_b \int_x^1 dz \frac{K_{ab}(\alpha_s(\mu^2))}{1-z} \tilde{f}_b(x/z,\mu^2) - \sum_b \int_0^1 dz \frac{K_{ab}(\alpha_s(\mu^2))}{1-z} \tilde{f}_b(x,\mu^2) \tag{3.11}$$

In the region $1 > z > z_M$, we expand the momentum-weighted parton density as,

$$\tilde{f}_b(x/z,\mu^2) = \tilde{f}_b(x,\mu^2) + (1-z)\frac{\partial \tilde{f}_b(x,\mu^2)}{\partial \ln x} + O(1-z)^2 \tag{3.12}$$

Then, we find that the contribution to the equation from the non-resolvable region is of order $O(1-z_M)$, and thus, up to $O(1-z_M)$, we have,

$$\sum_b \int_x^1 dz \frac{K_{ab}(\alpha_s(\mu^2))}{(1-z)_+} \tilde{f}_b(x/z,\mu^2)$$

$$= \sum_b \int_x^{z_M} dz \frac{K_{ab}(\alpha_s(\mu^2))}{1-z} \tilde{f}_b(x/z,\mu^2) - \sum_b \int_0^{z_M} dz \frac{K_{ab}(\alpha_s(\mu^2))}{1-z} \tilde{f}_b(x,\mu^2) \tag{3.13}$$

Next, we consider the contributions to the evolution equations 3.4 from the other two terms, D_{ab} and R_{ab}. The R_{ab}, being at most logarithmic for $z \to 1$ combined with the first term on the right-hand side of equation contribution can be combined with the first term on the right hand side of equation 3.13, yields a contribution to the evolution proportional to $\tilde{f}_b(x/z,\mu^2)$. The D_{ab} contribution, using the $\delta(1-z)$, yields a contribution to the evolution proportional to $\tilde{f}_b(x,\mu^2)$. Thus, we can express the derivative of $\tilde{f}_a(x,\mu^2)$ with respect to $\ln\mu^2$ as,

$$\frac{\partial f_a(x,\mu^2)}{\partial \ln \mu^2} = \sum_b \int_x^{z_M} dz \left(K_{ab}(\alpha_s(\mu^2))\frac{1}{1-z} + R_{ab}(\alpha_s(\mu^2),z) \right) \tilde{f}_b(x/z,\mu^2)$$

$$+ \sum_b \left\{ \int_x^1 dz D_{ab}(\alpha_s(\mu^2))\delta(1-z) - \int_0^{z_M} dz K_{ab}(\alpha_s(\mu^2))\frac{1}{1-z} \right\} \tilde{f}_b(x,\mu^2) \tag{3.14}$$

The first line in equation 3.14 contains contributions to evolution from real parton emission, while the second line contains contributions from virtual corrections. It is convenient to define the kernels in the bracket of the first line as the real-emission branching probabilities $P_{ab}^{(R)}(\alpha_s,z)$,

$$P_{ab}^{(R)}(\alpha_s,z) = \frac{K_{ab}(\alpha_s)}{1-z} + R_{ab}(\alpha_s,z) \tag{3.15}$$

The real-emission branching probabilities $P_{ba}^{(R)}(\alpha_s,z)$ are derived from the splitting functions $P_{ba}(\alpha_s,z)$ by subtracting the $\delta(1-z)$ terms and replacing the plus-distribution $1/(1-z)_+$ by $1/(1-z)$. Consequently, the evolution of the momentum-weighted parton density can be expressed as,

$$\frac{\partial \tilde{f}_a(x,\mu^2)}{\partial \ln \mu^2} = \sum_b \int_x^{z_M} dz P_{ba}^{(R)}(\alpha_s(\mu^2),z)\tilde{f}_b(x/z,\mu^2)$$

$$+\sum_b \left\{ \int_x^1 dz D_{ab}(\alpha_s(\mu^2))\delta(1-z) - \int_0^{z_M} dz \frac{K_{ab}(\alpha_s(\mu^2))}{1-z} \right\} \tilde{f}_b(x,\mu^2) \tag{3.16}$$

The terms in the second line of this equation, which account for virtual corrections, are addressed through the use of the momentum sum rule.

3.3 Applying the Momentum Sum Rule

The momentum sum rule states that the total momentum carried by all partons in a hadron is conserved during the evolution process. Expressing this principle in terms of the splitting functions we get,

$$\sum_c \int_0^1 z P_{ca}(\alpha_s(\mu^2),z) dz = 0 \quad \text{(for any } a\text{)} \tag{3.17}$$

Which we need to eliminate the D-terms in the evolution equations in favor of the K-terms and R-terms. Inserting the momentum sum rule into the evolution equations, by subtracting the momentum sum integral in the second line of equation 3.16. We know that the D_{ab} and K_{ab} terms in this equation are diagonal in flavor and therefore, by interchanging indices, we obtain from equation 3.16

$$\frac{\partial \tilde{f}_a(x,\mu^2)}{\partial \ln \mu^2} = \sum_b \int_x^{z_M} dz P_{ba}^{(R)}(\alpha_s(\mu^2),z)\, \tilde{f}_b(x/z,\mu^2)$$

$$+\sum_c \left\{ \int_x^1 dz D_{ca}(\alpha_s(\mu^2))\delta(1-z) - dz \int_0^{z_M} K_{ca}(\alpha_s(\mu^2)) \frac{1}{1-z} \right\} \tilde{f}_a(x,\mu^2) \tag{3.18}$$

Let us now use again the decomposition for $P_{ca}(\alpha_s(\mu^2),z)$ in the last line of this equation. We observe that the D_{ca} term in $P_{ca}(\alpha_s(\mu^2),z)$ cancels against the first term in the curly bracket in equation 3.18, while the R_{ca} term in $P_{ca}(\alpha_s(\mu^2),z)$ may be restricted to the region $z < z_M$, up to order $O(1-z_M)$. Finally, the K_{ca} term in $P_{ca}(\alpha_s(\mu^2),z)$ may be combined with the second term in the curly bracket in equation 3.18. Putting pieces together we get,

$$\frac{\partial \tilde{f}_a(x,\mu^2)}{\partial \ln \mu^2} = \sum_b \int_x^{z_M} dz P_{ba}^{(R)}(\alpha_s(\mu^2),z)\, \tilde{f}_b(x/z,\mu^2)$$

$$-\sum_c \left\{ \int_0^{z_M} dz K_{ca}(\alpha_s(\mu^2)) \frac{1}{1-z} + \int_0^{z_M} dz R_{ca}(\alpha_s(\mu^2),z) \right\} \tilde{f}_a(x,\mu^2) \tag{3.19}$$

We thus recognize, by using equation 3.15, that the evolution equations 3.16 can be written as

$$\frac{\partial \tilde{f}_a(x,\mu^2)}{\partial \ln \mu^2} = \sum_b \int_x^{z_M} dz P_{ba}^{(R)}(\alpha_s(\mu^2),z)\, \tilde{f}_b(x/z,\mu^2)$$

$$- \int_0^{z_M} dz z P_{ba}^{(R)}(\alpha_s(\mu^2),z)\, \tilde{f}_a(x,\mu^2) \tag{3.20}$$

3.4 The Sudakov Form Factor

Let's introduce another factor, the Sudakov form factor,

$$\Delta_a(z_M,\mu^2,\mu_0^2) = \exp\left(-\sum_b \int_{\mu_0^2}^{\mu^2} \frac{d\mu'^2}{\mu'^2} \int_0^{z_M} dz P_{ba}^{(R)}(\alpha_s(\mu'^2),z) \right) \tag{3.21}$$

The Sudakov form factor $\Delta_a(z_M,\mu^2,\mu_0^2)$ has the interpretation of probability for parton a to undergo no branching between evolution scale μ_0 and evolution scale μ. Noting that,

$$\frac{\partial\Delta_a(z_M,\mu^2,\mu_0^2)}{\partial\ln\mu^2} = -\Delta_a(z_M,\mu^2,\mu_0^2)\sum_b\int_0^{z_M} dz\,P_{ba}^{(R)}(\alpha_s(\mu^2),z) \tag{3.22}$$

we obtain from equation 3.20 (removing z_M and μ_0^2 from the argument list for better readability),

$$\begin{aligned}\frac{\partial\tilde{f}_a(x,\mu^2)}{\partial\ln\mu^2} &= \sum_b\int_x^{z_M} dz\,P_{ab}^{(R)}(\alpha_s(\mu^2),z)\,\tilde{f}_b(x/z,\mu^2)\\ &\quad+\frac{1}{\Delta_a(\mu^2)}\frac{\partial\Delta_a(\mu^2)}{\partial\ln\mu^2}\tilde{f}_a(x,\mu^2)\end{aligned} \tag{3.23}$$

This evolution equation can be written in a form similar to equation 3.4, but now in terms of real-emission probabilities $P_{ab}^{(R)}$ and Sudakov form factors,

$$\frac{\partial}{\partial\ln\mu^2}\left(\frac{\tilde{f}_a(x,\mu^2)}{\Delta_a(\mu^2)}\right) = \sum_b\int_x^{z_M} dz\,P_{ab}^{(R)}(\alpha_s(\mu^2),z)\,\frac{\tilde{f}_b(x/z,\mu^2)}{\Delta_a(\mu^2)} \tag{3.24}$$

Integrating this equation we obtain, with $\Delta_a(\mu_0^2)=1$,

$$\tilde{f}_a(x,\mu^2) = \Delta_a(\mu^2)\tilde{f}_a(x,\mu_0^2)+\sum_b\int_{\mu_0^2}^{\mu^2}\frac{d\mu'^2}{\mu'^2}\Delta_a(\mu'^2)\int_x^{z_M} dz\,P_{ab}^{(R)}(\alpha_s(\mu'^2),z)\,\tilde{f}_b(x/z,\mu'^2) \tag{3.25}$$

We recognize that introducing the Sudakov form factor has led to an equation which is an integral equation of Fredholm type,

$$f(t) = f_0(t)+\lambda\int_a^b K(t,y)f(y)dy. \tag{3.26}$$

This is finally the form of the evolution equation that we need to calculate the behaviour of the partons inside the hadron in the Drell-Yan process. We can solve it numerically making use of the famous monte carlo technique! We actually need to rewrite equation 3.25 one last time by keeping angular ordering in mind.

In simple terms, when a high-energy quark or gluon radiates a softer gluon, the angular ordering rule dictates that each subsequent emission must occur at a smaller angle relative to the direction of the initial high-energy parton than the previous emission. This is because gluons are emitted coherently from all colored charges involved in the process, and the interference between different emission amplitudes leads to a suppression of radiation at large angles.

The reason we need this is because when a particle involved in the strong force, like a quark, shoots out other particles, the direction of these sprays gets more focused each time. It's like a sprinkler that starts spraying water all over but gradually starts to spray in a tighter stream. This idea is really important for Monte Carlo programs that try to mimic these particle sprays. In these simulations, every new spray has to be more straight and narrow than the one before. We write the branching equation for the evolution of collinear (partons along the direction of motion of the parent particle) and TMD distribution as,

$$\begin{aligned}\tilde{A}_a(x,k_t,\mu^2) &= \Delta_a(\mu^2)A_a(x,k_t,\mu_0^2)+\sum_b\int\frac{d^2\mathbf{q}'}{\pi q'^2}\Delta_a(\mu^2)\frac{\alpha_s}{2\pi}\Delta_a(q'^2)\Theta(\mu^2-q'^2)\Theta(q'^2-\mu_0^2)\\ &\quad\times\int_x^{z_M} dz\,P_{ab}^{(R)}(\alpha_s(q'^2),z)\tilde{A}_b(z,k_t+(1-z)q',q'^2)\end{aligned} \tag{3.27}$$

where $\tilde{A}$ is the momentum weighted distribution $\tilde{A}=xA$ and $A_a(x,k_t,\mu^2)$ the TMD distribution functions. k_t quantifies how much a parton is moving sideways (perpendicular to the beam direction) inside a fast-moving proton or neutron, so it is the transverse momentum of the parton.

3.5 Parton Branching Method with a Dynamic Resolution Scale

In practice, we will utilize the parton branching (PB) TMD methodology to describe Drell-Yan processes at low transverse momentum (p_T), which refers to the transverse momentum of the lepton pair, across a wide range of lepton pair masses (m_{ll}). To achieve this, we require next-to-leading order (NLO) hard scattering matrix elements, which we obtain from the MCatNLO method, an NLO event generator, which we will be discussing in the following section. These elements are then matched with TMD parton distributions and showers (the repeated splitting of partons creates an extensive branching of emitted particles) that result from PB evolution. Our results will demonstrate that the PB TMD distributions contribute significantly due to the intrinsic-k_T (the transverse momentum of the partons), even though most of the small-k_T contribution arises from PB evolution.

Looking at the PB evolution equations again for TMD parton distributions $\hat{A}_a(x,\mathbf{k},\mu^2)$ of flavor a, which are expressed as,

$$\hat{A}_a(x,\mathbf{k},\mu^2) = \Delta_a(\mu^2)A_a(x,k_T,\mu_0^2) + \sum_b \int \frac{d^2q'}{\pi q'^2}\Delta_a\left(\frac{\mu^2}{q'^2}\right)\Delta_a\left(\frac{\mathbf{q}'^2}{\mu_0^2}\right)\Theta(\mu^2-\mathbf{q}'^2)\Theta(\mathbf{q}'^2-\mu_0^2)$$

$$\times \int_x^{z_M}\frac{dz}{z}P_{ab}^{(R)}(\alpha_s(q'^2),z)\hat{A}_b\left(\frac{x}{z},\mathbf{k}+(1-z)\mathbf{q}',\mathbf{q}'^2\right) \tag{3.28}$$

where $\mathbf{k}$ and $\mathbf{q}'$ are 2-dimensional momentum vectors, z_M is the soft resolution scale, z is the longitudinal momentum fraction in the branching, $P_{ab}^{(R)}(\alpha_s,z)$ are the resolvable splitting functions, and Δ_a are the Sudakov form factors defined by,

$$\Delta_a(z_M,\mu^2,\mu_0^2) = \exp\left(-\sum_b\int_{\mu_0^2}^{\mu^2}\frac{d\mathbf{q}'^2}{q'^2}\int_0^{z_M}dz\,z\,P_{ab}^{(R)}(\alpha_s(\mathbf{q}'^2),z)\right) \tag{3.29}$$

The evolution equation incorporates soft-gluon angular ordering, with the branching variable $\mathbf{q}'^2$ related to the transverse momentum q_T of the emitted parton at the branching by,

$$q_T = (1-z)|\mathbf{q}'| \tag{3.30}$$

It has also been established that angular ordering is crucial for the TMD distribution derived from the evolution equation to be well-defined and to remain independent of the choice of the soft-gluon resolution scale $z_M = 1-\varepsilon$ as $\varepsilon \to 0$. In contrast, ordering by p_T can lead to ambiguities in the definition of the TMD, particularly as $z \to 1$.

Analogously to the case of ordinary parton distribution functions, the distribution $\hat{A}_a(x,k_T,\mu^2)$ at the starting scale μ_0 of the evolution, in the first term on the right hand side of the evolution equation is a non-perturbative boundary condition to the evolution equation and is to be determined from experimental data. For clarity, let's simplify the description of the Transverse Momentum Dependent (TMD) parton distribution function, $\hat{A}_a(x,k_T,\mu^2)$, which is parameterized as follows,

$$\hat{A}_{0,a}(x,k_T,\mu_0^2) = f_{0,a}(x,\mu_0^2)\cdot\exp\left(-\frac{|\mathbf{k}|^2}{2\sigma^2}\right)/(2\pi\sigma^2) \tag{3.31}$$

Here, the width of the Gaussian distribution, denoted as $\sigma = \frac{q_s}{\sqrt{2}}$. This parameter is the same for all types of partons and does not depend on their momentum fraction x which were determined in the study [45]. The quantity q_s represents the intrinsic transverse momentum parameter, which provides a measure of the average inherent sideways motion of the partons within the hadron.

The 'width of the Gaussian' in this context symbolizes the uncertainty or spread in the partons' momentum due to their confinement in the hadron, often referred to as Fermi motion. For instance, in a proton made up of 'up-up-down' (uud) quarks, as we inject energy into the system, the simple uud configuration becomes more complex. We observe more valence quarks and other partons, implying that the original step-like distribution of the quarks' momenta evolves into a smoother, more continuous distribution. The variable k_T, therefore, reflects the degree to which we have distorted the original Fermi distribution by pumping energy into the hadron, altering its internal partonic structure and the number of observable particles.

Another thing to note is that when we include the concept of angular ordering, it introduces a mathematical condition to determine if a gluon emission is 'resolvable', meaning it has enough energy to be detected separately from the parton that emitted it. The condition is given by $z < z_M(\mu')$ with,

$$z_M(\mu') = 1 - \frac{q_0}{\mu'} \tag{3.32}$$

Here, q_0 is the minimum transverse momentum needed for an emission to be resolved, and μ' is the evolution scale, a parameter related to the energy scale of the collision process. Equation 3.32 helps us visualize and distinguish between the resolvable and non-resolvable regions. When plotted, these regions form distinct areas on a graph with axes μ' and z.

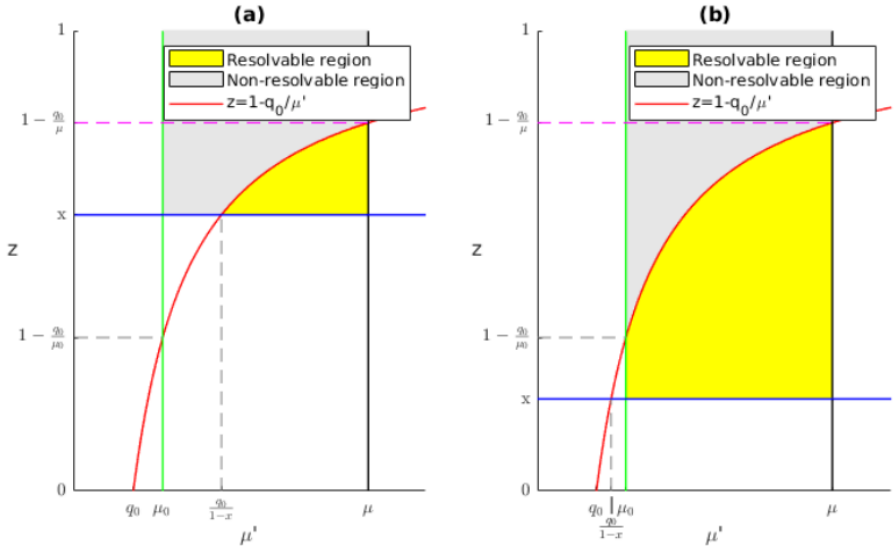

Figure 3.1: Graphical representation of the angular ordering condition and the distinguishable regions for resolvable and non-resolvable emissions in parton branching processes. The vertical axis represents the longitudinal momentum fraction z, while the horizontal axis represents the scale μ'. Graph (a) shows the scenario where $1 \geq x \geq 1 - q_0/\mu_0$, and graph (b) shows the case for $1 - q_0/\mu_0 > x > 0$. The red line denotes the critical angular ordering condition $z_M(\mu') = 1 - q_0/\mu'$, separating the resolvable (yellow) and non-resolvable (gray) regions [18].

In Figure 3.1, the yellow region represents the resolvable region, while the gray region represents the non-resolvable region, as indicated in the figure's legend. The red line denotes the dynamic z_M that we will be using, which implies that only the resolvable region is considered. Consequently, our Sudakov form factor will only include the perturbative components. In reference [45], similar research was conducted as in this thesis, but with a key difference in the use of z_M. There, a fixed z_M was employed, as illustrated by the purple line in Figure 3.1. Using a fixed z_M means also considering non-perturbative

Sudakov factors (gray region), which is a particular modeling approach. The inclusion of the non-perturbative Sudakov factor was based on the logical assumption that the Sudakov form factor must have a non-perturbative component or region. In this thesis, we will be using the dynamical z_M (in chapter 5 we will discuss this again).

4 Drell-Yan Process

This chapter is mostly based on reference [8].

Now that we have an expression for the behaviors of partons inside hadrons, let's examine a specific process we briefly discussed earlier: the Drell-Yan process. This chapter aims to understand this process and explore why it is used to study quarks and gluons. Let's begin by examining the Feynman diagram and describing what happens.

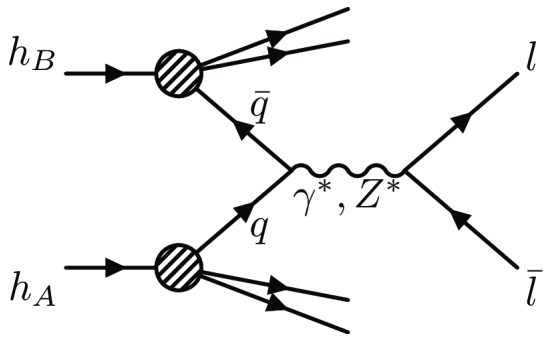

Figure 4.1: Feynman diagram illustrating the Drell-Yan process where quark (q) and antiquark ($\bar{q}$) from hadrons h_A and h_B annihilate, producing a virtual photon (γ^*) or Z-boson (Z^*), which then decays into a lepton (l) and antilepton ($\bar{l}$) pair [20].

In the figure above, we see h_A and h_B, which represent two colliding hadrons (for example, two protons). Next, we have the partons, denoted by q for a quark and $\bar{q}$ for an antiquark. The quark emanates from one hadron and the antiquark from the other. These partons interact with each other, leading to a particle exchange, which can be either a virtual photon (a particle intermediate state not directly observable but facilitating the interaction between the quark and antiquark) or a Z-boson. From the quark-antiquark annihilation, a pair of leptons is produced. In the diagram, l represents a lepton, such as an electron, while $\bar{l}$ represents the corresponding antilepton, such as a positron. Moving forward, we will only consider the case where a Z-boson is exchanged, and we will disregard the virtual photon case.

In the parton model, we can express the cross section σ_{AB} for producing a lepton pair in a collision between beam A and target B using the parton distribution functions $f_q(x)$ and $f_{\bar{q}}(x)$, summing over all possible quark-antiquark combinations as follows,

$$\sigma_{AB} = \sum_q \int dx_1 dx_2 f_q(x_1) f_{\bar{q}}(x_2) \hat{\sigma}_{q\bar{q}\to l\bar{l}} \tag{4.1}$$

where $\hat{\sigma}_{q\bar{q}\to l\bar{l}}$ is the subprocess cross section of the Drell-Yan process. The agreemant between this theoretical expression and the measured Drell-Yan cross sections at the Large Hadron Collider (LHC) has validated the parton model approach. This was notably the first time a hadron-hadron cross section could be derived from first principles (refers to the fundamental concepts or assumptions at the core

of a subject). The expression also survived the inclusion of perturbative QCD corrections, where all divergences in the Drell-Yan corrections are factored into the renormalized parton distributions. The updated cross section expression, incorporating the scale of the hard scattering process (high-energy collision between particles that results in a large momentum transfer), is,

$$\sigma_{AB} = \sum_q \int dx_1 dx_2 f_q(x_1, M^2) f_{\bar{q}}(x_2, M^2) \hat{\sigma}_{q\bar{q}\to l\bar{l}} \tag{4.2}$$

Here, M^2 denotes the large invariant mass squared of the lepton pair. This value is significant because it sets the scale at which the hard scattering process is probed. In perturbative QCD, M^2 is important as it governs the running of the strong coupling constant and influences the evolution of parton distribution functions.

When calculating the cross section σ_{AB} for producing lepton pairs in particle collisions, it's also essential to consider the finite contributions that remain after the singularities (divergences) have been factored into the parton distributions. These contributions are the actual perturbative corrections to the cross section at order $\mathcal{O}(\alpha_s)$,

$$\sigma_{AB} = \sum_q \int dx_1 dx_2 f_q(x_1, M^2) f_{\bar{q}}(x_2, M^2) \hat{\sigma}_{q\bar{q}\to l\bar{l}} \left[\hat{\sigma}_0 + a\hat{\sigma}_1 + a^2\hat{\sigma}_2 + \ldots\right] \tag{4.3}$$

with $a = \frac{\alpha_s(M^2)}{2\pi}$. This formula is not just for one specific situation but can be used for many different high-energy collisions. Most processes have been worked out to the next-to-leading order in perturbation theory, which includes the term $\hat{\sigma}_1$. The Drell-Yan process has even been calculated up to next-to-next-to-leading order. We will discuss the Drell-Yan cross section in detail in the coming sections and then talk about how this applies to Z boson production in high-energy proton-antiproton ($p\bar{p}$) collisions. We will also try to keep the explanation more general and avoid delving too deeply into the mathematics, as we did in the first chapter, because this could lead us into many topics that are not our main focus.

4.1 Lowest Order Cross Section: Quark-Antiquark Annihilation

Let's start by examining the lowest-order cross section for quark-antiquark annihilation into a lepton pair,

$$\hat{\sigma}(q(p_1), \bar{q}(p_2) \to l\bar{l}) = \frac{4\pi\alpha^2}{3(p_1+p_2)^2} \frac{1}{N} Q_p^2 \tag{4.4}$$

Here, p denotes the momentum of the incoming quarks, $1/N$ is a color factor (we must keep color in our calculations because annihilation can only occur when the color of the quark matches that of the antiquark), and Q_p is the electric charge factor of the quarks. Since the incoming quark and antiquark can have a spectrum of collision energies, it is more appropriate to consider the differential lepton pair mass distribution. Therefore, the subprocess cross section for producing a lepton pair of mass M is given by,

$$\frac{d\hat{\sigma}}{dM^2} = \frac{\sigma_0}{N} Q_p^2 \delta((p_1+p_2)^2 - M^2) \tag{4.5}$$

with $\sigma_0 = \frac{4\pi\alpha^2}{3M^2}$. Utilizing this equation in the parton model gives the cross section for this process,

$$\frac{d\sigma}{dM^2} = \int_0^1 dx_1 dx_2 \sum_q f_q(x_1) f_{\bar{q}}(x_2) \frac{d\hat{\sigma}}{dM^2}(q\bar{q} \to l\bar{l}) \tag{4.6}$$

Considering now the rapidity y of the lepton pair. Rapidity is a concept used to describe the angle and relative velocity of a particle along the beam axis in a collider experiment. It provides a way to quantify

how fast and in what direction a particle is moving relative to the beamline, which is now expressed in terms of the parton momentum fractions as,

$$y = \frac{1}{2} \ln \frac{x_1}{x_2} \tag{4.7}$$

the double-differential cross section becomes,

$$\frac{d^2\sigma}{dM^2 dy} = \frac{\sigma_0}{N} \left[\sum_q Q_p^2 \left(f_q(x_1) f_{\bar{q}}(x_2) \right) \right] \tag{4.8}$$

The double-differential cross section provides a measure of how the likelihood of lepton pair production varies with both the invariant mass M^2 of the pair and their rapidity y. This is significant because it allows us to potentially measure the distribution functions of quarks and antiquarks within the hadrons involved in the collision by analyzing the rapidity and mass of the lepton pairs. To further our analysis, we must consider the transverse momentum q_T of the partons, which is a crucial variable in our dataset. This analysis is represented by a new expression for the cross section,

$$\sigma = \sum_{a,b} \int d^2 q_{T,1} d^2 q_{T,2} \int dx_1 dx_2 A_a(x_1, q_{T,1}, \mu^2) A_b(x_2, q_{T,2}, \mu^2) \hat{\sigma}_{ij}(x_1, x_2, q_{T,1}, q_{T,2}, \mu^2, Q^2) \tag{4.9}$$

By measuring the resulting lepton pairs, we are effectively reverse engineering the collision process to understand the initial state of the quarks and antiquarks. Next, we aim to apply this understanding to the Drell-Yan process to derive the cross section in terms of q_T, using the same reverse logic.

4.2 Adding Perturbative QCD Corrections on Drell-Yan Calculations

In this section, we calculate the $\mathcal{O}(\alpha_s)$ corrections to the parton model Drell-Yan cross section. We begin by considering the parton-level Drell-Yan cross section for the leading-order process $q(p_1) + \bar{q}(p_2) \to l\bar{l}$,

$$M^4 \frac{d\sigma}{dM^2} = \frac{4\pi\alpha^2}{3N} \tau \hat{\mathscr{F}}(\tau) \tag{4.10}$$

with $\tau = \frac{M^2}{(p_1+p_2)^2}$ and $\hat{\mathscr{F}}(\tau) = Q_p^2 \delta(1-\tau)$, which is the expression we previously encountered in Equation 4.5 for a single flavor of quark with charge Q_p. Generally, $\hat{\mathscr{F}}$ has a perturbative expansion in powers of the strong coupling,

$$\hat{\mathscr{F}}(\tau) = \hat{\mathscr{F}}_0(\tau) + \frac{\alpha_s}{2\pi} \hat{\mathscr{F}}_1(\tau) + \dots \tag{4.11}$$

The diagrams contributing to $\mathcal{O}(\alpha_s)$ are given in figure 4.2. We can categorize them into three classes of contributions,

- (a) Virtual gluon corrections to the leading-order contribution $\hat{\mathscr{F}}_1^{q\bar{q},V}$
- (b) Real gluon corrections $\hat{\mathscr{F}}_1^{q\bar{q},R}$
- (c) Quark-gluon scattering process $\hat{\mathscr{F}}_1^{qg}$

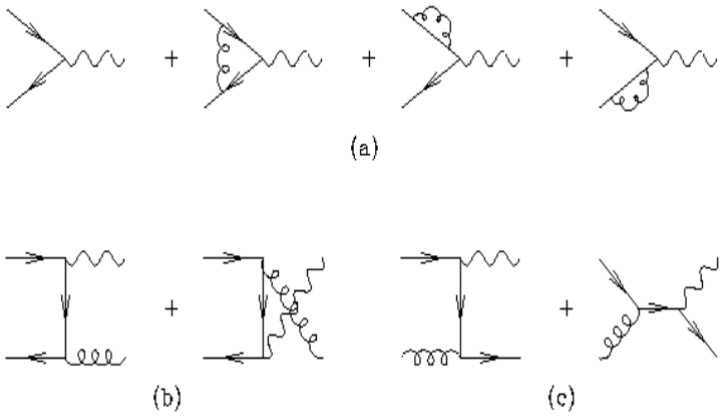

Figure 4.2: Contributions to the Drell-Yan cross section at the first order in the strong coupling constant α_s. The diagrams show (a) virtual corrections, and (b) real emission processes involving gluons, contributing to the next-to-leading order (NLO) corrections of the cross-section [8, p.307].

As in Chapter 1, we will account for ultraviolet divergences from the loop integrals, infrared divergences from the contribution (both real and virtual) of soft gluons (gluons with low energy or momentum), and divergences from the splitting of the initial-state partons. We utilize regularization again in the space-time dimension of $4-2\varepsilon$ and reintroduce μ^2. The result, ignoring terms of $\mathscr{O}(\varepsilon)$ or higher, is,

$$\hat{\mathscr{F}}_1^{q\bar{q}} = \hat{\mathscr{F}}_1^{q\bar{q},V} + \hat{\mathscr{F}}_1^{q\bar{q},R} = Q_p^2 \frac{\alpha_s(\mu^2)}{2\pi}\left[2\left(-\frac{1}{\varepsilon} - \ln 4\pi + \gamma_E + \ln\frac{M^2}{\mu^2}\right)P_{qq}^{(0)}(\tau) + D_q(\tau)\right] \tag{4.12}$$

$$\hat{\mathscr{F}}_1^{qg} = Q_p^2 \frac{\alpha_s(\mu^2)}{2\pi}\left[2\left(-\frac{1}{\varepsilon} - \ln 4\pi + \gamma_E + \ln\frac{M^2}{\mu^2}\right)P_{qg}^{(0)}(\tau) + D_g(\tau)\right] \tag{4.13}$$

with,

$$D_q(z) = C_F\left[4(1+z^2)\left(\frac{\ln 1-z}{1-z}\right)_+ - 2\frac{1+z^2}{1-z}\ln z + \delta(1-z)\left(\frac{2\pi^2}{3} - 8\right)\right] \tag{4.14}$$

$$D_g(z) = T_R\left[(z^2+(1-z)^2)\ln\frac{(1-z)^2}{z} + \frac{1}{2} + 3z - \frac{7}{2}z^2\right] \tag{4.15}$$

When the bare parton distributions, which must be convoluted with the $\hat{\mathscr{F}}_1^{q\bar{q}}$ and $\hat{\mathscr{F}}_1^{qg}$ functions, are replaced by scale-dependent 'renormalized' distributions, the divergences exactly cancel. We find that the parton distribution function is given by,

$$q(x,\mu^2) = q_0(x) + \frac{\alpha_s(\mu^2)}{2\pi}\left(-\frac{1}{\varepsilon} - \ln 4\pi + \gamma_E\right)\int_x^1 \frac{d\xi}{\xi}\left[P_{qq}^{(0)}\left(\frac{x}{\xi}\right)q_0(\xi) + P_{qg}^{(0)}\left(\frac{x}{\xi}\right)g_0(\xi)\right] + \mathscr{O}(\alpha_s^2) \tag{4.16}$$

This equation is precisely the DGLAP evolution equation! Now, writing the full cross section would be quite lengthy, so we will not present it here, but it is detailed in [22]. What we do know is that the magnitude of the $\mathscr{O}(\alpha_s))$ correction depends on the mass of the lepton pair and the overall collision energy. This means that we can work backwards, using what we can measure experimentally to gain information about the quarks and antiquarks. Fortunately, the production of Z-bosons in a Drell-Yan process in pp collisions is one of the most precisely measured processes at high energies at the LHC, so the information we need is trustworthy and already known.

4.3 Calculating The Drell-Yan Transverse Momentum

To work backwards, we will be needing the transverse momentum like we mentioned and this will be done by employing the method developed in [25, 26]. According to this method, the hard scattering matrix element for DY production is generated at next-to-leading order (NLO) in perturbation theory using the MCatNLO program [27], and this is matched with the TMD distributions [28] constructed in [21, 29] by using suitable subtraction terms to deal with partons moving in nearly the same direction (collinear) or with very low energy (soft). A detailed study of these subtractions terms is performed in the appendix of Ref. [30].

The method [25, 26] is designed to take into account both the transverse-momentum recoils in the parton shower evolution and the nonperturbative intrinsic-k_T contributions [31, 32, 33]. It is implemented in the Monte Carlo event generator Cascade [34, 35]. Besides DY production, the method has also been applied to jet production [36, 37]. This approach has been found to describe the measured DY transverse momentum distributions well in the region of low to moderate transverse momenta. The region of high transverse momenta requires the additional technique [39, 39, 40] to take into account the contribution of multiple jet radiation. In the following, we will limit ourselves to considering the low transverse-momentum region.

For our computation of the DY transverse momentum, we will use the integrated and TMD NLO parton densities from the set PB-NLO-2022 [41], obtained from fits to deep inelastic scattering precision data [42] using the xFitter package [43, 44]. We employ the factorization scale μ, defined as $\mu = \frac{1}{2}\sum_i \sqrt{m_i^2 + p_{t,i}^2}$, where the sum is over all the final state particles. This scale helps us to distinguish between short-distance interactions, which involve high-energy processes and can be described by perturbation theory, and long-distance effects, such as the binding of quarks and gluons within protons. When calculating transverse momentum in line with the PB-TMD distributions, the factorization scale μ in the hard-scattering process is set to the mass of the Drell-Yan system, $\mu = m_{ll}$. In scenarios involving real emissions, the scale is determined by the aforementioned formula which accounts for the mass and transverse momentum of all final state particles [25, 45].

In our calculations, while the primary focus is on QCD, it is essential not to overlook the effects of QED. Particularly, we must consider scenarios where high-speed leptons emit photons. This phenomenon is significant as it can influence the final state of particle interactions and affect the accuracy of our predictions. QED effects are crucial when dealing with lepton pairs produced in high-energy collisions, such as those observed in the Drell-Yan process. The emission of photons by leptons can lead to observable changes in the energy and momentum distribution of the final state particles. These emissions, known as final state radiation (FSR), can alter the apparent invariant mass of the lepton pair and alter the experimental measurements if not correctly accounted for. Hence, including QED corrections helps ensure that theoretical predictions align closely with experimental data [25].

The PB TMD approach which we employ to compute the DY transverse momentum can be compared with the traditional CSS approach [46]. TMD distributions determined from DY data using CSS are given in [47, 48, 49, 50, 51, 54]. Both PB and CSS distributions are accessible from the library [53, 54]. A first discussion of the relationship between the two approaches is given in [55]. A deeper comparison between them will be important, and will be an interesting subject for future investigations.

4.4 Summary

Because hadrons are composite particles, their collisions are inherently complex. The difficulty lies in the involvement of low-energy (or equivalently, long-distance or long-time) regimes where the application of perturbation theory for Quantum Chromodynamics (QCD) becomes infeasible. Nonetheless, there's a workaround: factorization. This method hinges on the capacity to disentangle short-distance effects, which are amenable to perturbative calculations, from long-distance effects. Without hadrons, long-time effects could simply be negated through unitarity. However, hadrons complicate this, making it impossible. The best achievable solution is to separate long- and short-time effects. Thus, a factorized expression can be derived, linking measurable hadronic quantities to partonic quantities that are calculable through perturbation theory. The demarcation between long-time and short-time (or low-energy and high-energy) introduces an artificial factorization scale. For the inclusive cross section of a collision between two hadrons, the factorized formula encapsulates the parton distribution functions (PDFs) of the interacting partons within the hard process and the hard-scattering function that characterizes the hard interaction. The PDFs are evaluated at the factorization scale, while the hard-scattering function is calculated using the strong coupling at the renormalization scale and also depends on the factorization scale. A pivotal equation we've derived in this chapter is the Dokshitzer-Gribov-Lipatov-Altarelli-Parisi (DGLAP) evolution equation, a renormalization group equation for (momentum-weighted) PDFs, delineating their evolution with the mass scale. The DGLAP equations are formulated in terms of splitting functions, which describe the likelihood of a parton splitting into two other partons at a given mass scale.

5 Study of Drell-Yan transverse momentum at varying masses in the PB TMD methodology: dynamical resolution scale and intrinsic transverse momentum

As part of the PBO-NLO-2022 dataset, which includes the Transverse Momentum Dependent (TMD) distributions used in our calculations, we will analyze data using a series of Les Houches Event (LHE) files. Each LHE file is crucial for Monte Carlo simulations [1] in particle physics experiments, capturing the output from event generators. Our initial assessments have focused on how the quantity of LHE files affects computational workload and simulation accuracy.

Note that at the end of Chapter 3, we clarified which z_M we used and highlighted that we will be using the dynamical z_M, as this has not been researched yet. In reference [45], a similar study was conducted to examine the dependence of k_T on the mass of the lepton pair, resulting in findings that showed no dependence. In this thesis, the idea is to investigate whether removing the non-perturbative Sudakov factor will yield the same results, specifically the mass independence in our results.

In this new study, we aim to enhance our understanding of the scaling variable q_s by fitting CMS data [19] across various mass ranges using the Parton Branching (PB) method, now incorporating a dynamical $z_{\max}$. This modification allows for a more precise adaptation to the variable conditions of parton momentum fractions, thereby providing a more accurate representation of parton dynamics under various experimental scenarios. Additionally, we will examine the impact of setting different $p_{T,\max}$ values, which effectively truncates the number of data points or the range of the transverse momentum, across varying masses.

5.1 Analyzing The Number of LHE Files used

Our objective in this part was to determine whether results obtained from processing a large number of LHE files align with those derived from a smaller, more manageable set. If the outcomes from both sets agree, it would indicate that a less extensive dataset can yield reliable results. This finding would be significant as it would allow us to make accurate predictions while conserving both time and computational resources.

For our analysis, we will explore various mass window ranges and adjust some parameters to determine their impact on the mass of the lepton pair. Specifically, we will vary q_0, performing calculations at $q_0 = 1$ GeV and $q_0 = 0.5$ GeV. Additionally, we will adjust q_s, starting from $q_s = 0.0001$ GeV, then increasing to $q_s = 0.1$ GeV, and continuing in increments of 0.1 GeV up to 1.6 GeV for $q_0 = 0.5$ GeV and up to 2 GeV for $q_0 = 1$ GeV. We will also explore how varying the p_T range affects our results, setting $p_{T,\max}$ values of 5, 10, and 15 GeV.

[1] The solution of the evolution equation applying a Monte Carlo method can be found in reference [21, p.8-10]

These variations cover all the parameters we will be adjusting. The mass windows for our analysis are set as follows,

$$m_{ll} = [50 \text{ to } 76, 76 \text{ to } 106, 106 \text{ to } 170, 170 \text{ to } 350, 350 \text{ to } 1000]\text{GeV} \tag{5.1}$$

This comprehensive approach allows us to thoroughly assess any dependencies these parameters might have on the mass of the lepton pair. Of course, we won't be displaying all the plots we produced, as there are too many. However, this is not an issue, because they all follow the same structure. By understanding one example, we can generalize to all the plots. We will discuss the results for $q_0 = 0.5$ GeV and $q_0 = 1.0$ GeV separately, as we will see notable differences that merit individual attention.

5.1.1 Influence of the number of LHE files for $q_0 = 0.5$ GeV

Let's examine the calculations for $q_s = 0.2$ GeV, $q_0 = 0.5$ GeV, and $p_{T,\text{max}} = 10$ GeV. We will compare the results from both the large LHE file set and the smaller LHE file set, and plot these out as seen on figure 5.1.

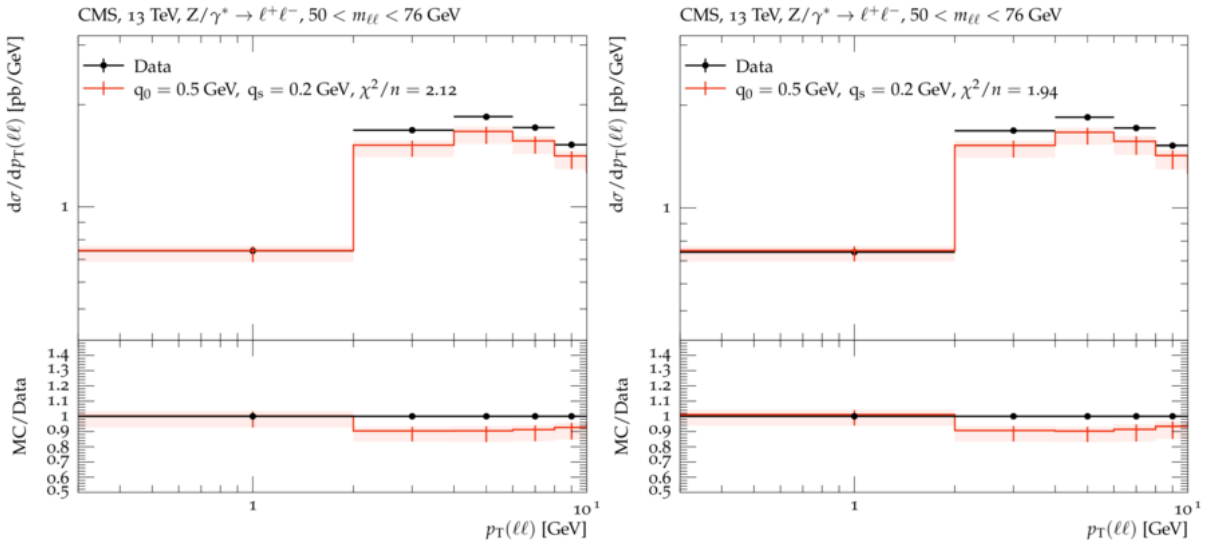

Figure 5.1: Comparison of differential cross sections for lepton pair production using two different LHE file sizes across the mass window of 50 GeV $\leq m_{ll} \leq$ 76 GeV. The figures display the experimental data (black points) against the theoretical predictions (red lines) for minimal $q_s = 0.2$ GeV, $q_0 = 0.5$ GeV, and maximum transverse momentum, $p_{T,\text{max}} = 10$ GeV. The left graph uses the large LHE file set, and right graph utilizes the smaller LHE file set.

It shows the differential cross section (on the y-axix denotes as $d\sigma/dp_T$), which is the probability per unit transverse momentum (on the x-axis denoted $p_T(ll)$) interval of producing lepton pairs in the lepton mass window (m_{ll}) from 50 GeV to 76 GeV. The measurement is performed at a center-of-mass energy of 13 TeV. The black points represent the actual experimental data with error bars indicating the uncertainty in the measurements. The red line represents theoretical predictions made using our parameters.

The lower panel of the graph provides the ratio of the Monte Carlo simulation prediction to the actual data (MC/Data). A value of 1 in this ratio would mean a perfect match between the simulation and the data. Variations above or below 1 indicate the discrepancies between the predicted and observed

results, reflecting how accurately the theoretical model with the chosen parameters q_0 and q_s describes the experimental data.

Finally, the chi-square per degree of freedom (χ^2/n) value is a statistical measure used to assess the goodness of fit of a theoretical model to observed data. It's calculated with,

$$\chi^2 = \sum_{i,k} (m_i - \mu_i) C_{ik}^{-1} (m_k - \mu_k) \tag{5.2}$$

with m_i being the measurement and μ_i being the prediction for data point i. The covariance matrix C_{ik} is decomposed into a component describing the uncertainty in the measurement, $C_{ik}^{\text{meas.}}$, and the statistical and scale uncertainties in the prediction,

$$C_{ik} = C_{ik}^{\text{meas.}} + C_{ik}^{\text{model-stat.}} + C_{ik}^{\text{scale}} \tag{5.3}$$

The covariance matrix of the measurement is taken directly from the supplementary material provided by CMS.

A χ^2/n value close to 1 indicates a good fit; the model predictions are in good agreement with the observed data, within the limits of statistical fluctuations. If the χ^2/n value is significantly greater than 1, it suggests that the model may not be adequately describing the data, or it could also mean that the uncertainties have been underestimated. Conversely, a value much less than 1 might indicate that the model fits the data too well and that the uncertainties might be overestimated.

If the data is not dependent on a variable, then we expect the minimal χ^2 value to be approximately the same even when changing the variable. So let's look if the number of LHE files has any effect and we will be using $p_{T,max} = 5, 10, 15$ GeV (we will just do this for every $p_{T,max}$ so we can be sure of our conclusion) to check this with different q_s values. So the idea is to look which q_s value has a minimal χ^2 value and plot this in function of the mass (we use the mean mass of each window to be able to plot it) and thus we get the figures 5.2-5.4.

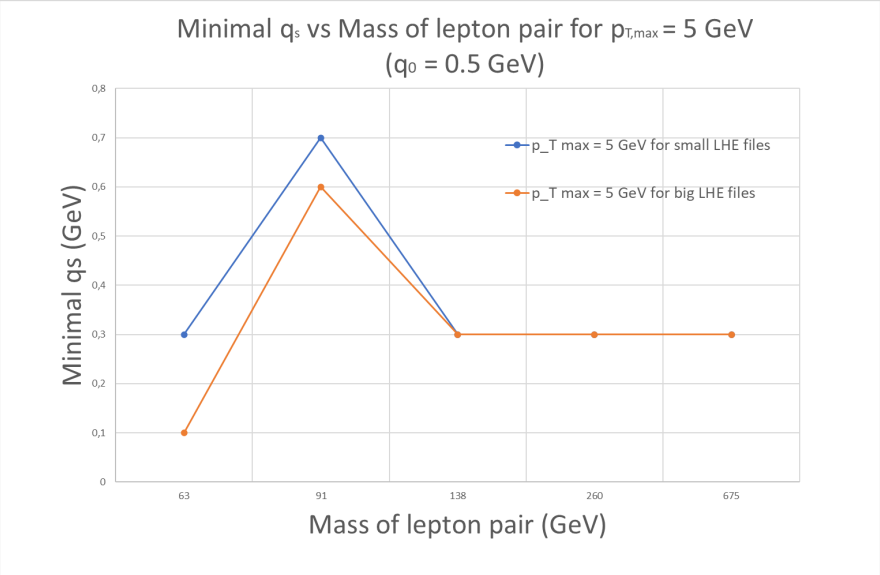

Figure 5.2: Variation of minimal q_s values against the mean mass of the lepton pair for $p_{T,\text{max}} = 5$ GeV settings for $q_0 = 0.5$ GeV. The plot illustrate how the sensitivity of the minimal χ^2 values varies with the lepton pair mass and the influence of $p_{T,\text{max}}$ cut-off.

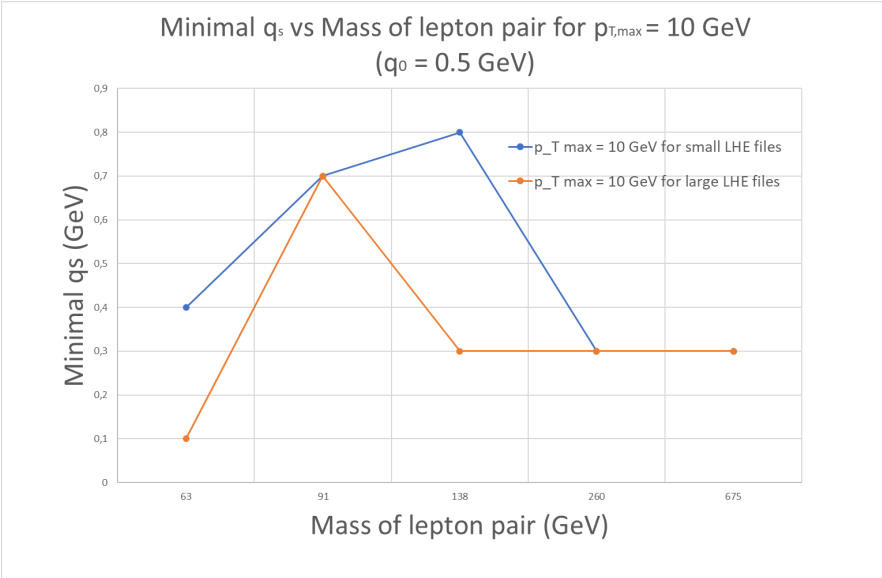

Figure 5.3: Variation of minimal q_s values against the mean mass of the lepton pair for $p_{T,\max} = 10$ GeV settings for $q_0 = 0.5$ GeV. The plot illustrate how the sensitivity of the minimal χ^2 values varies with the lepton pair mass and the influence of $p_{T,\max}$ cut-off.

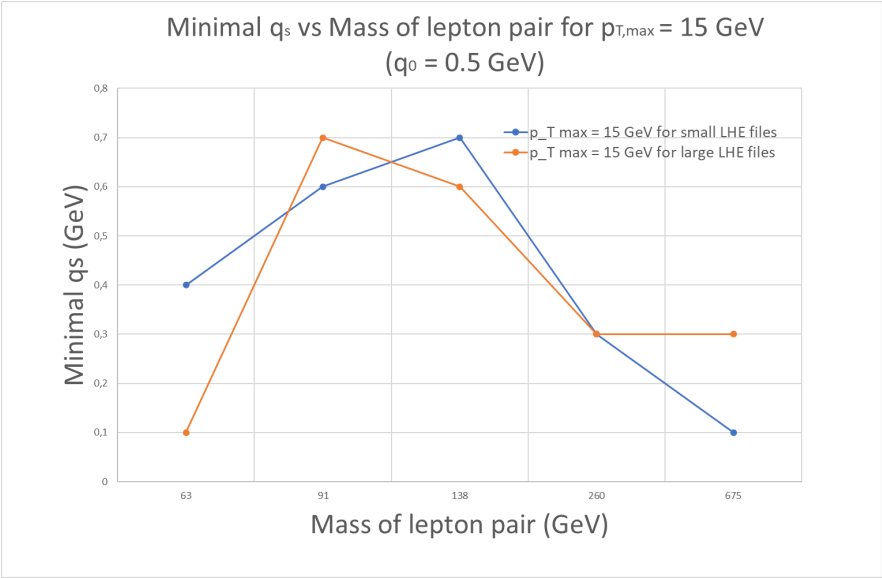

Figure 5.4: Variation of minimal q_s values against the mean mass of the lepton pair for $p_{T,\max} = 15$ GeV settings for $q_0 = 0.5$ GeV. The plot illustrate how the sensitivity of the minimal χ^2 values varies with the lepton pair mass and the influence of $p_{T,\max}$ cut-off.

Observing the plots, the behavior of the individual graphs appears notably unstable. Additionally, the minimal χ^2 values for both lines do not seem to match cleanly, except at $p_{T,\max} = 5$ GeV. Notably, we observe a peak typically occurring in the second or third mass window, specifically at $m_{ll} = 76$ to 106 GeV or $m_{ll} = 106$ to 170 GeV. These peaks could be attributed to several factors:

- The proximity of the peaks to the mass of the Z boson (which is around 90 GeV [57]) suggests that resonant production might be influencing the distributions. At resonance, the production cross-section is significantly enhanced, which could explain the observed peaks. The initial state configuration characterized by q_0 may directly impact the kinematics and dynamics of the particle

interactions. A higher q_0 value might shift the energy distribution available for particle production, moving beyond the resonance or threshold energies where certain particles or states are more likely to be produced. For example, if the peak at $q_0 = 0.5$ GeV corresponds to a resonant production such as the Z boson, increasing q_0 to 1.0 GeV could result in a distribution that either overshoots the resonance peak or affects the efficiency of detecting these states due to altered kinematics. Notably, this peak does not occur with $q_0 = 1$ GeV. Another thing to note is that the peaks of the blue and orange lines on the graphs do not always overlap. This could be because the mass of the Z boson is close to the boundary of the second and third mass windows and the mass can vary to become higher than 106 GeV due to its momentum and this could place the peak on the third mass window instead of the second.

- The detector's resolution or the analysis's sensitivity to changes in q_0 might also play a crucial role. Higher values of q_0 may lead to broader or shifted peaks that are less distinguishable from the background, especially if the experimental setup or the data analysis techniques are optimized for a certain energy range.

5.1.2 Influence of the number of LHE files for $q_0 = 1.0$ GeV

Following the same protocol as outlined in the previous section, we now shift our focus to the case where $q_0 = 1.0$ GeV. Plotting the calculations for the Drell-Yan cross section and plotting these out, we get figure 5.5.

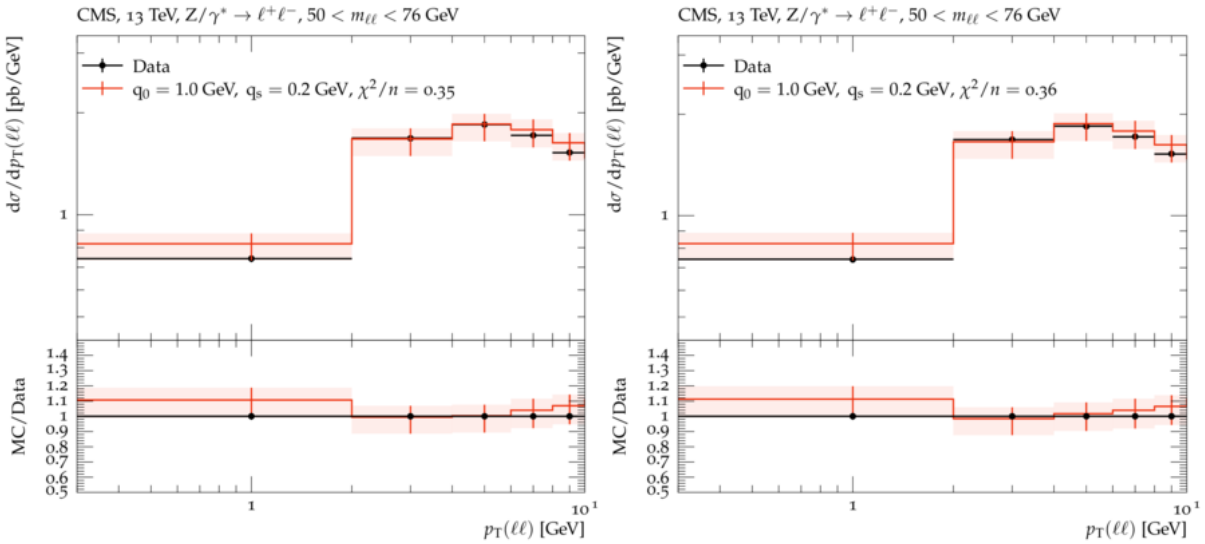

Figure 5.5: Comparison of differential cross sections for lepton pair production using two different LHE file sizes across the mass window of 50 GeV $\leq m_{ll} \leq$ 76 GeV. The figures display the experimental data (black points) against the theoretical predictions (red lines) for minimal $q_s = 0.2$ GeV, $q_0 = 1.0$ GeV, and maximum transverse momentum, $p_{T,max} = 10$ GeV. The left graph uses the large LHE file set, and right graph utilizes the smaller LHE file set.

Again, if the data is independent of these parameters, we would expect the minimal χ^2 values to remain consistent across measurements. To illustrate this, we have plotted the minimal χ^2 for each q_s value as a function of the mass of the lepton pair, as shown in Figures 5.6 through 5.8.

Upon examining the plots, it becomes apparent that, in general, the minimal χ^2 values match or are

quite close to each other for $q_0 = 1.0$ GeV. This observation leads us to conclude that utilizing the smaller set of LHE files yields results comparable to those obtained using the larger set, with the added benefit of time efficiency. Throughout the three plots, we observe that the minimal χ^2 starts around 1.0 but increases as the mass of the lepton pair rises (reaching a maximum around 1.5). This indicates that our uncertainty in the data grows as we move to higher masses. This behavior is logical because, when considering the mass windows for m_{ll}, we cover a much wider range for higher masses (50 to 76 GeV compared to 350 to 1000 GeV), resulting in increased uncertainties for the same amount of data. However, our conclusion that there is no significant difference between using large or small LHE files remains unchanged. Compared to $q_0 = 0.5$ GeV, we observe that there is no peak, as previously explained.

Moving forward, we will use the smaller LHE file set for our analyses with $q_0 = 1.0$ GeV [2], as we have verified that the plots for both LHE file sizes yield consistent results in this setting. For $q_0 = 0.5$ GeV, we will analyze both sizes of LHE files due to observed unusual behavior, which prevents us from conclusively determining LHE size independence. We will next explore how the cutoff for maximum transverse momentum, $p_{T,\max}$, influences our results across various q_s values within different mass window ranges.

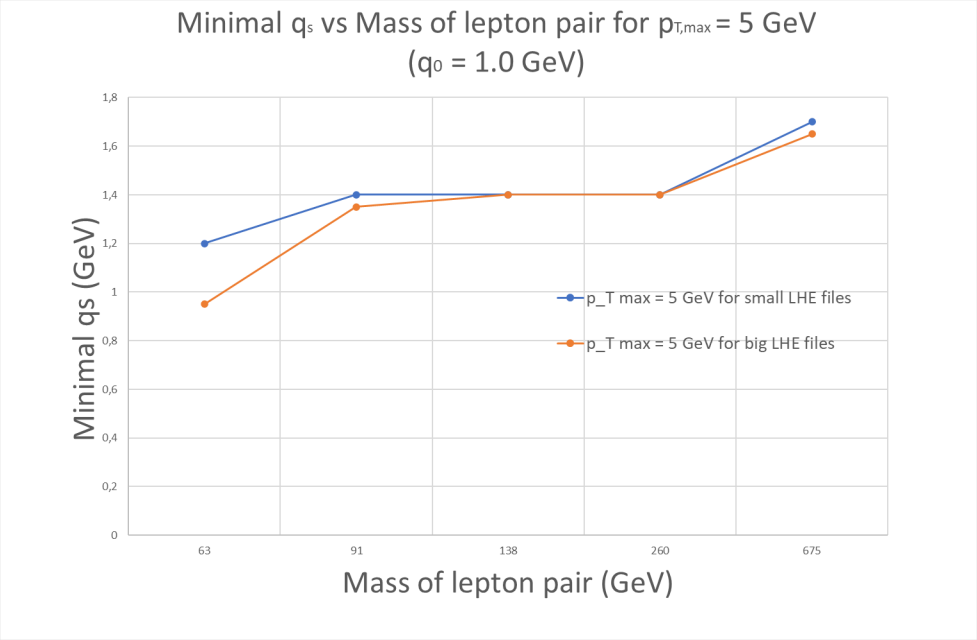

Figure 5.6: Variation of minimal q_s values against the mean mass of the lepton pair for $p_{T,\max} = 5$ GeV settings for $q_0 = 1.0$ GeV. The plot illustrate how the sensitivity of the minimal χ^2 values varies with the lepton pair mass and the influence of $p_{T,\max}$ cut-off.

[2] Just to cover all bases, I'll throw in the plot for the big file set too in the next section.

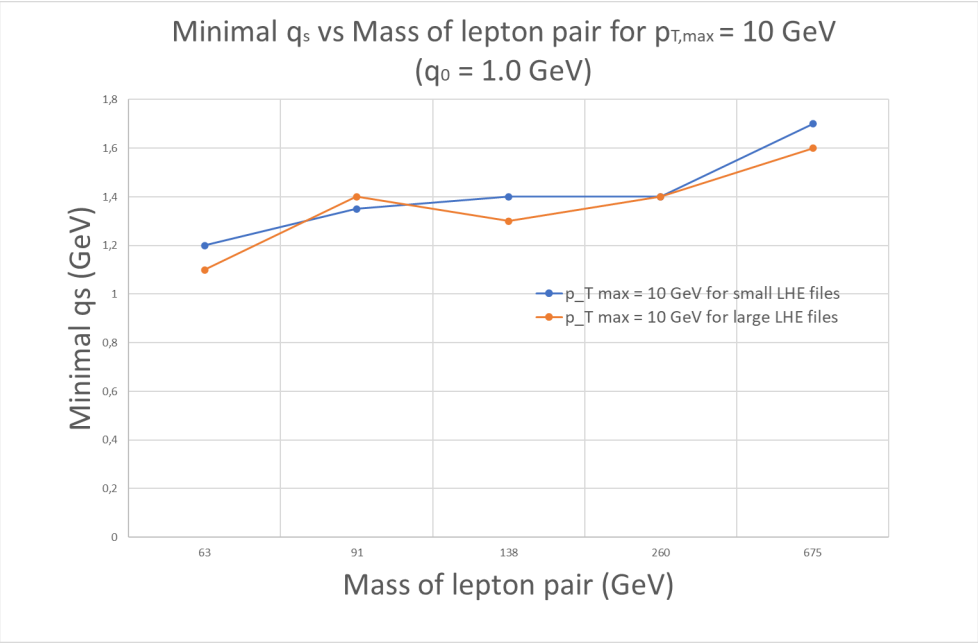

Figure 5.7: Variation of minimal q_s values against the mean mass of the lepton pair for $p_{T,\max} = 10$ GeV settings for $q_0 = 1.0$ GeV. The plot illustrate how the sensitivity of the minimal χ^2 values varies with the lepton pair mass and the influence of $p_{T,\max}$ cut-off.

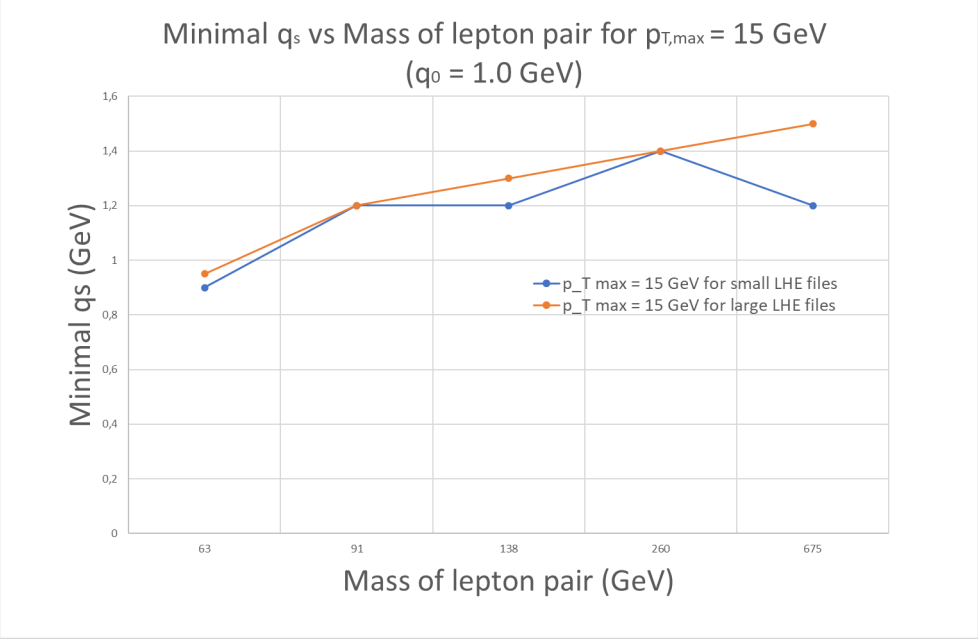

Figure 5.8: Variation of minimal q_s values against the mean mass of the lepton pair for $p_{T,\max} = 15$ GeV settings for $q_0 = 1.0$ GeV. The plot illustrate how the sensitivity of the minimal χ^2 values varies with the lepton pair mass and the influence of $p_{T,\max}$ cut-off.

5.2 Evaluating the Impact of $p_{T,max}$ Cuts Across Different q_s Values

As a refresher, varying q_s values alters the width of the Gaussian distributions, impacting the number of particles in our simulation. We aim to understand how applying a cut to $p_{T,max}$ influences our results

across different q_s values within various lepton pair mass (m_{ll}) windows. The initial plots from which we derive our χ^2/n values appear in figure 5.9 (these plots are merely illustrative samples from a larger set and this will be the same for $q_0 = 0.5$ GeV and $q_0 = 1.0$ GeV).

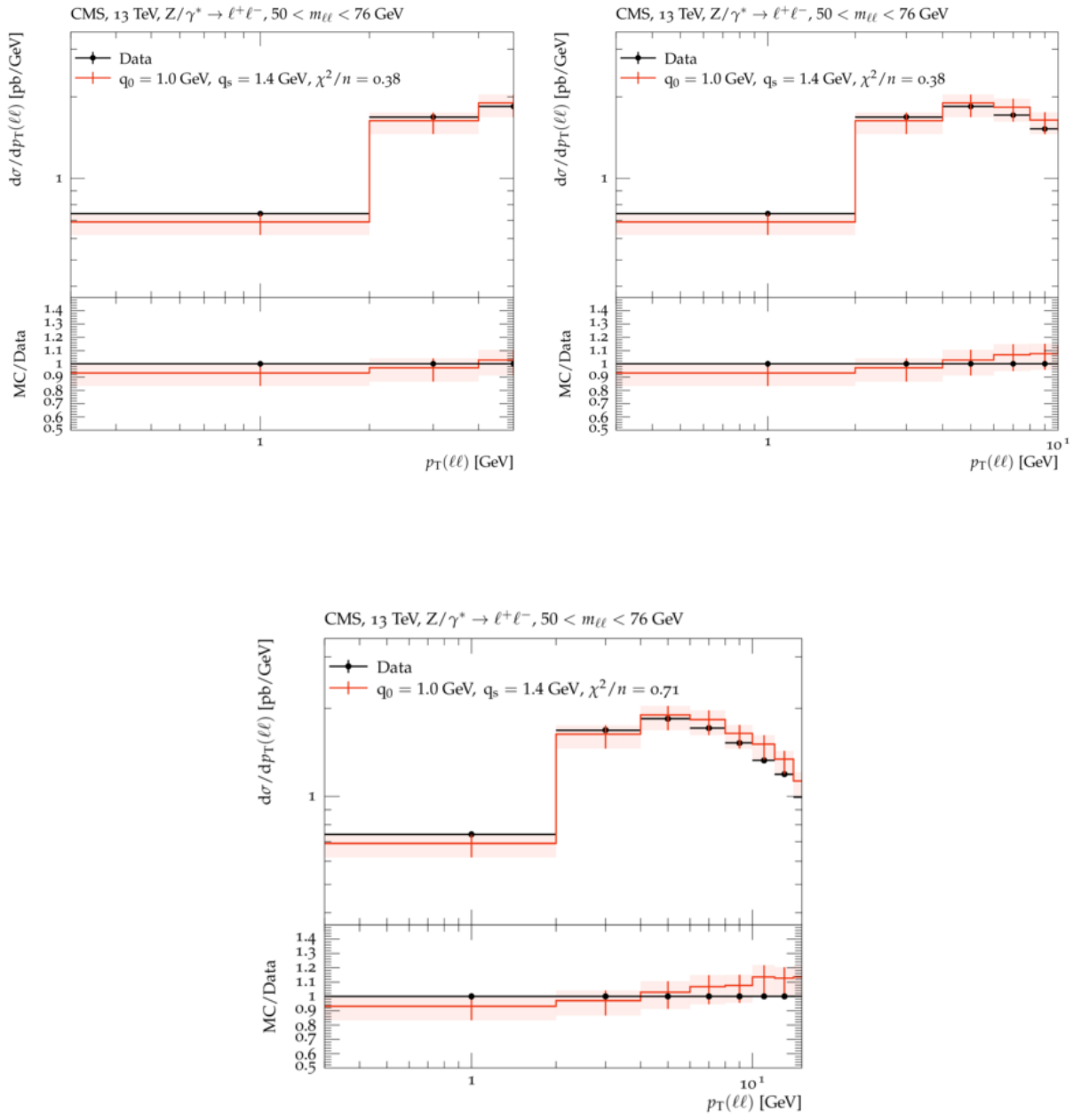

Figure 5.9: Comparison of differential cross-section plots for p_T distributions of lepton pairs with varying Gaussian widths (q_s values) at different transverse momentum cuts ($p_{T,max} = 5$ GeV for the top-left plot, $p_{T,max} = 10$ GeV for the plot underneath, and $p_{T,max} = 15$ GeV for the top-right plot), sampled from simulations for the mass window of $m_{ll} = 50$ to 76 GeV. These are illustrative examples representing the consistent trend observed across a broader data set.

As we can observe, a larger $p_{T,\text{max}}$ enables the inclusion of more data points. Let's now again talk about the q_0 values separately.

5.2.1 $p_{T,max}$ cut influence on $q_0 = 0.5$ GeV

Plotting the minimal χ^2 as a function of each q_s value, we observe trends as in figure 5.10-5.14 (for the large LHE set we will have similar looking plots).

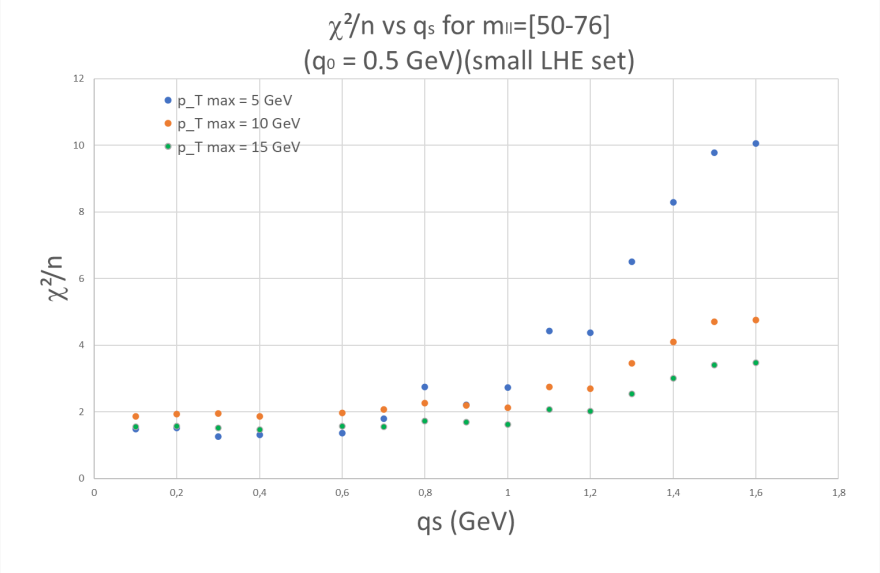

Figure 5.10: The minimal χ^2/n values across different q_s values for the lepton pair mass window of 50-76 GeV at $q_0 = 0.5$ GeV. Each series represents different transverse momentum cuts: blue for $p_{T,\max} = 5$ GeV, orange for $p_{T,\max} = 10$ GeV, and green for $p_{T,\max} = 15$ GeV.

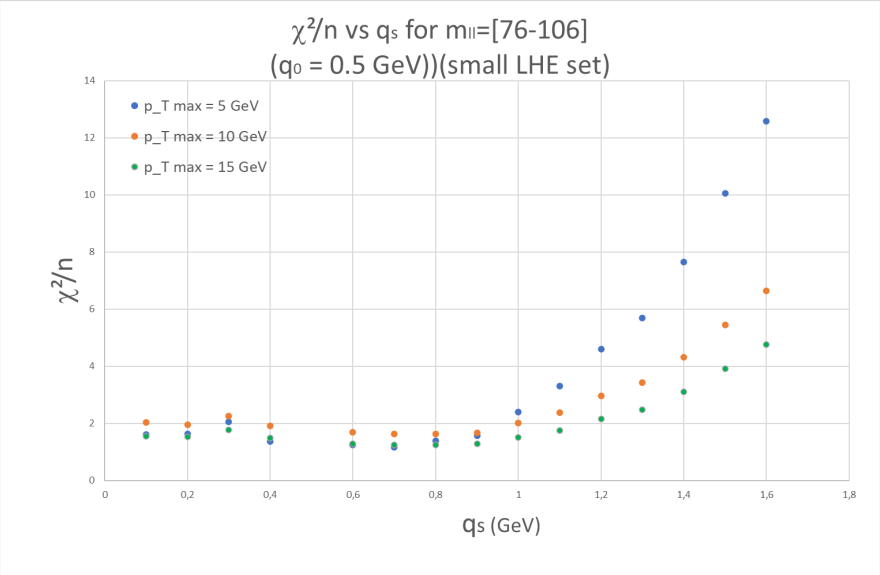

Figure 5.11: The minimal χ^2/n values across different q_s values for the lepton pair mass window of 76-106 GeV at $q_0 = 0.5$ GeV. Each series represents different transverse momentum cuts: blue for $p_{T,\max} = 5$ GeV, orange for $p_{T,\max} = 10$ GeV, and green for $p_{T,\max} = 15$ GeV.

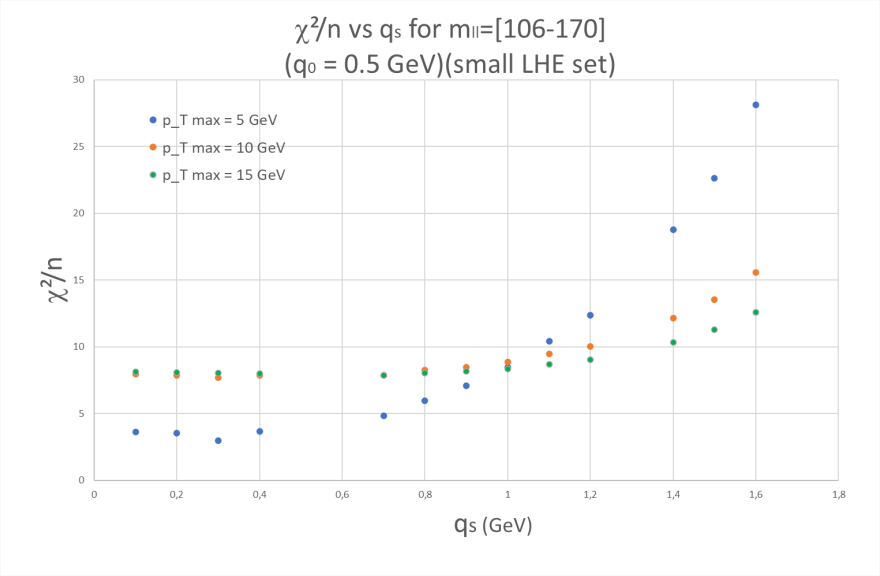

Figure 5.12: The minimal χ^2/n values across different q_s values for the lepton pair mass window of 76-106 GeV at $q_0 = 0.5$ GeV. Each series represents different transverse momentum cuts: blue for $p_{T,\max} = 5$ GeV, orange for $p_{T,\max} = 10$ GeV, and green for $p_{T,\max} = 15$ GeV.

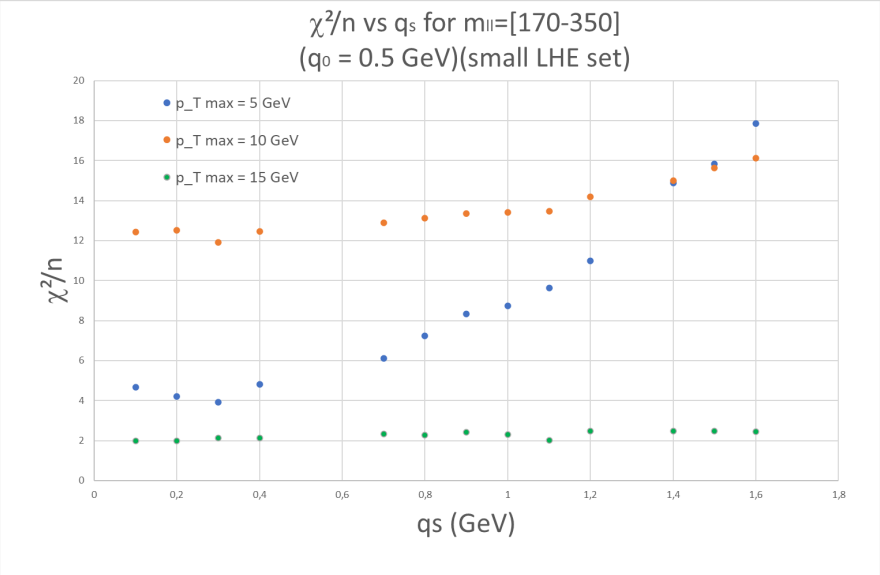

Figure 5.13: The minimal χ^2/n values across different q_s values for the lepton pair mass window of 170-350 GeV at $q_0 = 0.5$ GeV. Each series represents different transverse momentum cuts: blue for $p_{T,\max} = 5$ GeV, orange for $p_{T,\max} = 10$ GeV, and green for $p_{T,\max} = 15$ GeV.

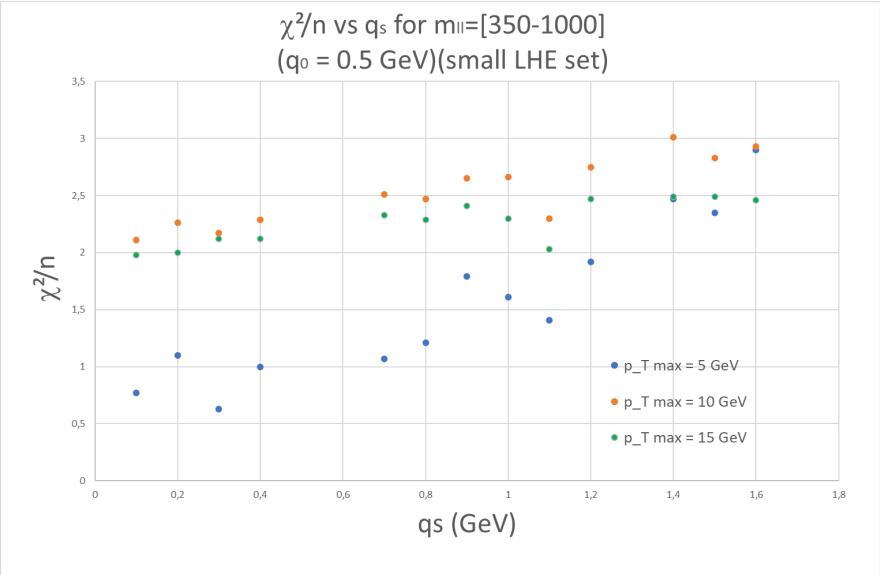

Figure 5.14: The minimal χ^2/n values across different q_s values for the lepton pair mass window of 350-1000 GeV at $q_0 = 0.5$ GeV. Each series represents different transverse momentum cuts: blue for $p_{T,\max} = 5$ GeV, orange for $p_{T,\max} = 10$ GeV, and green for $p_{T,\max} = 15$ GeV.

The uncertainty in Figure 5.10 begins to increase noticeably at around $q_s = 1.2$ GeV. The maximum χ^2 value reaches 3.47 for $p_{T,\max} = 15$ GeV and 4.75 for $p_{T,\max} = 10$ GeV. Notably, for $p_{T,\max} = 5$ GeV, the uncertainty spikes to 10.05, which is expected as the $p_{T,\max}$ cut limits the number of data points included in our calculations—more data typically yields greater accuracy. As q_s values increase, a clear dependency on $p_{T,\max}$ emerges.

Transitioning to higher mass ranges, the behavior begins to shift. In Figure 5.12, the differences in minimal χ^2 values among the three $p_{T,\max}$ settings become more pronounced; the most accurate results remain with $p_{T,\max} = 15$ GeV, but the second most precise shifts to $p_{T,\max} = 5$ GeV. By Figure 5.14, the ranks alter once again, with the most accurate calculations now associated with $p_{T,\max} = 5$ GeV. This suggests that for higher masses, a lower $p_{T,\max}$ yields more stable and reliable results.

At higher particle masses, using a lower maximum transverse momentum ($p_{T,\max}$) tends to yield more stable and reliable results. This setting helps to reduce unwanted background noise by filtering out less important, lower momentum particles. As a result, it allows us to focus more on the significant signals that come from higher mass particles.

Lower $p_{T,\max}$ settings also improve the accuracy of measurements, which is especially important when studying heavy particles. Accurate measurements are essential for correctly identifying these particles and separating them from irrelevant background activity. Additionally, a lower $p_{T,\max}$ reduces the complication of overlapping signals, known as pileup, in experiments conducted at colliders with very high rates of particle collisions. This reduction is advantageous because it helps to clarify the signals from high-mass particles, making them easier to detect and analyze.

Finally, we create similar plots to those in the previous sections, but in this case, we compare the effects of different $p_{T,\max}$ cuts.

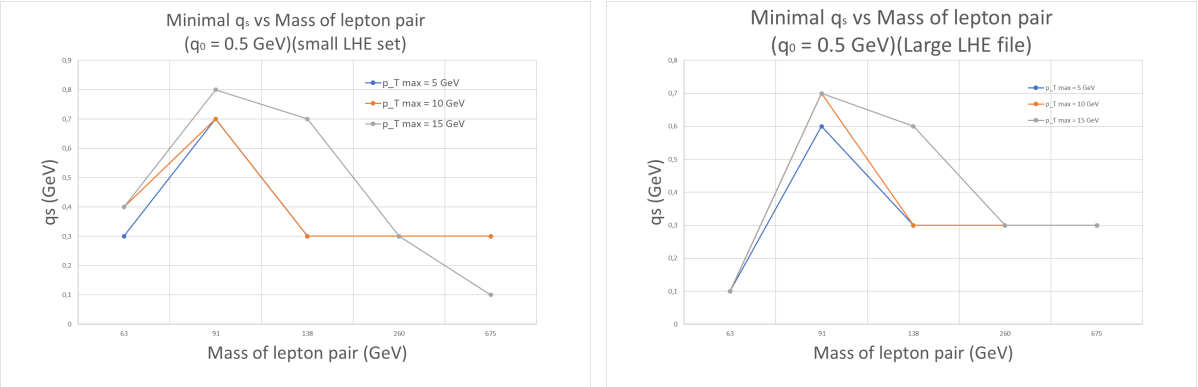

Figure 5.15: Comparison of the minimal q_s values as a function of lepton pair mass for two different sets of data at $q_0 = 0.5$ GeV. Left one is for the small set of LHE files and the right one is for the big set of LHE files. Each plot illustrates trends across different $p_{T,\max}$ cut-offs: 5 GeV, 10 GeV, and 15 GeV. Both plots demonstrate the influence of varying $p_{T,\max}$ on the minimal q_s values for lepton pairs within the mass range of 50 to 1000 GeV.

For $q_0 = 0.5$ GeV, as observed in Figure , the data predominantly forms a constant line with a peak occurring in the second or third mass window as we have seen multiple times before for $q_0 = 0.5$ GeV. Now the range of q_s for both sets is around the same. But the great news is that for both plots we find similar results, so the discussion about if the number of LHE files are important, we can say that for $q_0 = 0.5$ GeV, it is also not dependant of it.

5.2.2 $p_{T,max}$ cut influence on $q_0 = 1.0$ GeV

Now, plotting the minimal χ^2 as a function of each q_s value for $q_0 = 1.0$ GeV, we observe trends as in figure 5.16-5.18 (we will only show those plots where significant differences are observed between each).

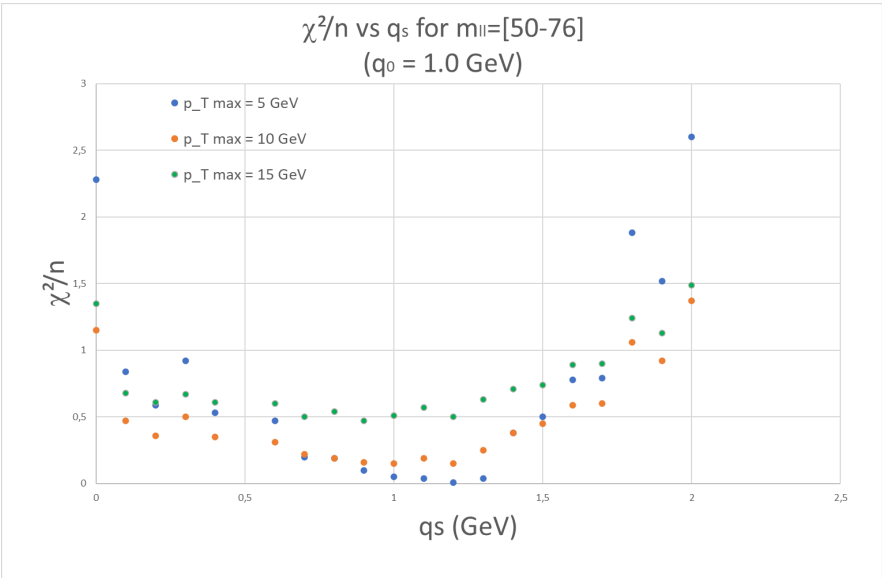

Figure 5.16: The minimal χ^2/n values across different q_s values for the lepton pair mass window of 50-76 GeV at $q_0 = 1.0$ GeV. Each series represents different transverse momentum cuts: blue for $p_{T,\max} = 5$ GeV, orange for $p_{T,\max} = 10$ GeV, and green for $p_{T,\max} = 15$ GeV.

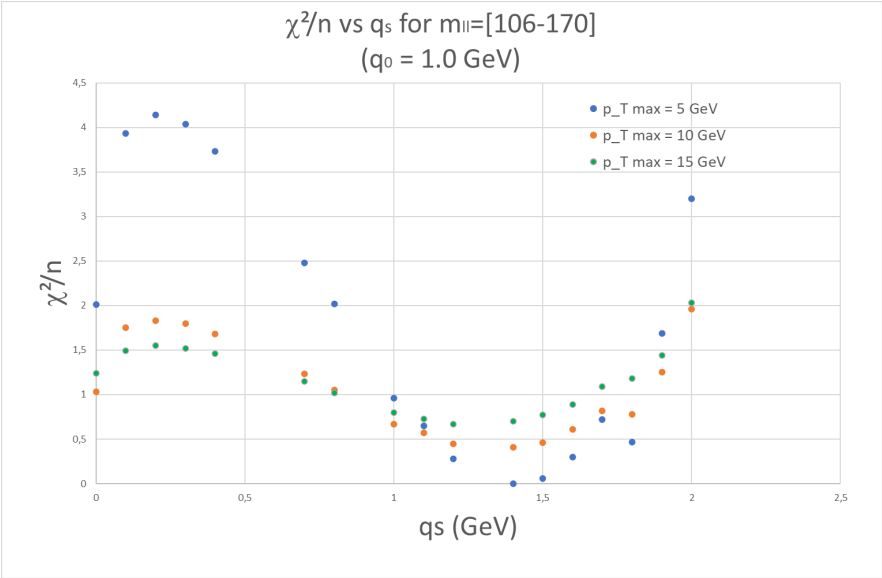

Figure 5.17: The minimal χ^2/n values across different q_s values for the lepton pair mass window of 106-170 GeV at $q_0 = 1.0$ GeV. Each series represents different transverse momentum cuts: blue for $p_{T,\max} = 5$ GeV, orange for $p_{T,\max} = 10$ GeV, and green for $p_{T,\max} = 15$ GeV.

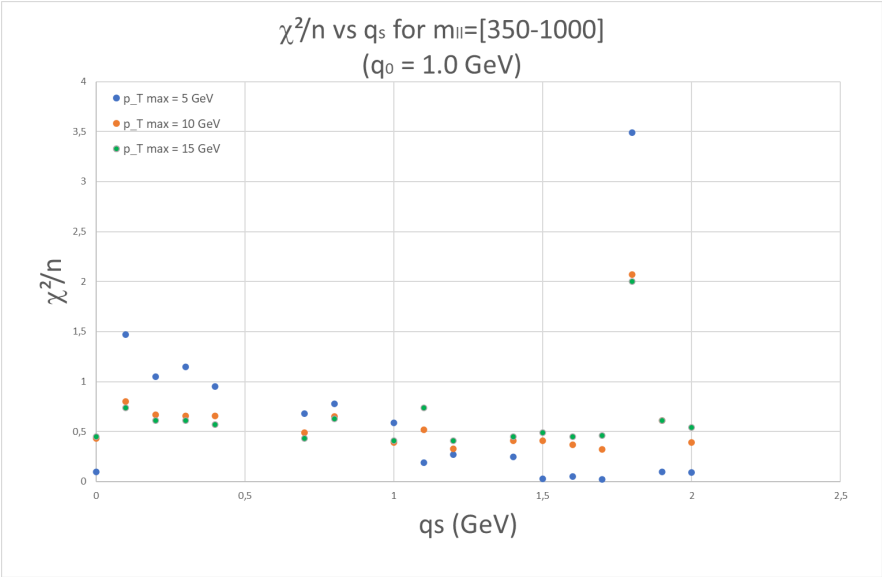

Figure 5.18: The minimal χ^2/n values across different q_s values for the lepton pair mass window of 350-1000 GeV at $q_0 = 1.0$ GeV. Each series represents different transverse momentum cuts: blue for $p_{T,\max} = 5$ GeV, orange for $p_{T,\max} = 10$ GeV, and green for $p_{T,\max} = 15$ GeV.

Looking at the figures above, we can observe a rank shift occurring again, but this time within the same plot. The behavior in Figure 5.16 is similar to that in Figure 5.10. However, examining Figures 5.17 and 5.18, we notice something special. In the plots at lower q_s values, $p_{T,\max} = 5$ GeV exhibits the most uncertainty. But as we move to higher q_s values, it becomes the least uncertain, effectively switching places with $p_{T,\max} = 15$ GeV. Apart from a few outliers, such as in Figure 5.17 at $q_s = 2$ GeV and in Figure 5.18 at $q_s = 1.7$ GeV, this trend is consistent in the last two plots. This could be the same behavior as we discussed earlier for $q_0 = 0.5$ GeV. However, because we are dealing with a higher q_0, which signifies a higher minimal emission transverse momentum, it likely means that at higher q_s values

(indicating more particles), we start observing more unnecessary emissions that add to the uncertainty. This explains why working with a lower $p_{T,\max}$ cut-off is more effective at higher q_s values.

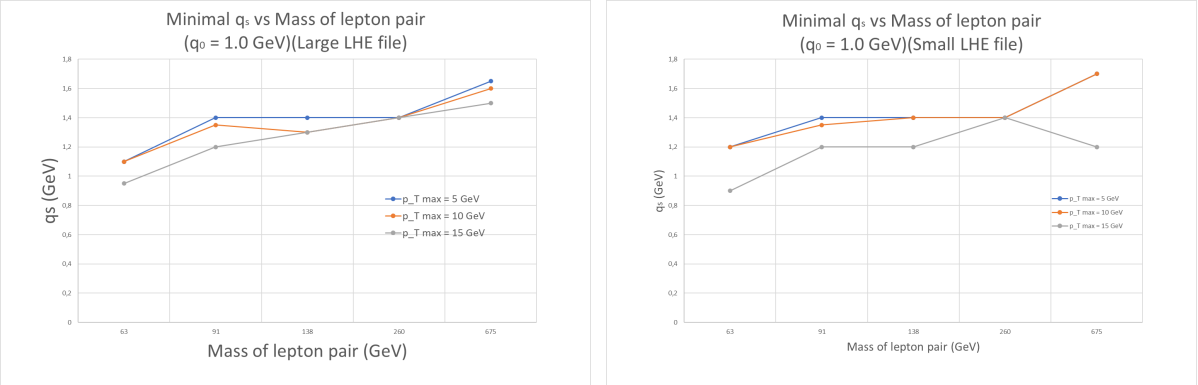

Figure 5.19: Comparison of the minimal q_s values as a function of lepton pair mass for two different sets of data at $q_0 = 1.0$ GeV. Left one is for the small set of LHE files and the right one is for the big set of LHE files. Each plot illustrates trends across different $p_{T,\max}$ cut-offs: 5 GeV, 10 GeV, and 15 GeV. Both plots demonstrate the influence of varying $p_{T,\max}$ on the minimal q_s values for lepton pairs within the mass range of 50 to 1000 GeV.

We previously noted that the LHE file size did not significantly impact our results for $q_0 = 1.0$ GeV, and as evidence we can see that the similarity between graphs in Figure 5.19. The minimal χ^2/n remains approximately constant across different settings, suggesting a lack of dependence on q_s across various mass windows. Given that q_s directly influences the Gaussian width, affecting the number of particles involved in the calculations, this independence implies that similar results can be achieved regardless of the particle count in the simulation. We can also clearly see that the lines remain constant across all mass windows (slightly increase), indicating that there is no (or atleast a mild) dependence on mass either.

Comparing the results for $q_0 = 0.5$ GeV and $q_0 = 1.0$ GeV, we find that the results are comparable if we disregard the peak and consider that for $q_0 = 0.5$ GeV, the data predominantly forms a constant line. However, a significant difference emerges in the minimal χ^2 values, which shift by approximately 1 when comparing Figure 5.15 for $q_0 = 0.5$ GeV and Figure 5.19 for $q_0 = 1.0$ GeV.

At a lower q_0 value of 0.5 GeV, the threshold for including emissions in the analysis is relatively low, allowing for a greater number of low-momentum emissions to contribute to the event. This typically results in a higher degree of background noise and potentially more fluctuations in the measured variables, which can contribute to a relatively constant but noisy line in the data distribution. Conversely, increasing q_0 to 1.0 GeV raises the kinematic threshold, effectively filtering out lower-momentum emissions that do not meet this criterion. This filtering can lead to a cleaner signal with fewer low-momentum background emissions, resulting in a more distinct and possibly more accurate depiction of the underlying physics processes, as reflected by a shifted χ^2 value.

The increase in q_0 likely reduces the overall complexity of the events by omitting less significant emissions, which can enhance the clarity and quality of the data. However, it also means that some real but low-momentum events are excluded from the analysis, which could potentially omit relevant physical phenomena present at lower momentum scales. Thus, the choice of q_0 must balance between achieving sufficient resolution to capture relevant physics and maintaining a manageable level of background noise.

6 Conclusion

In this thesis we have performed a study of non-perturbative strong-interaction effects in the transverse-momentum spectra of DY lepton pair production at the LHC. We have used the Parton Branching-Transverse Momentum Distribution methodology to obtain theoretical predictions for the DY transverse momentum distributions, and we have carried out a systematic comparison of these predictions with recent experimental measurements of the DY transverse momentum performed at the LHC in a broad range of DY invariant masses.

We have concentrated on the region of low transverse momenta, which is where the non-perturbative strong-interaction dynamics is expected to become important. The PB TMD methodology allows one to take this dynamics into account by introducing intrinsic transverse momentum distributions at low mass scales and studying their evolution to high mass scales in terms of appropriate generalizations of renormalization group equations. In this approach, the predictions for DY distributions thus depend on non-perturbative intrinsic transverse momentum parameters, and are otherwise determined by theory. In our work, by comparing the predictions with LHC experimental measurements, we have used the experimental data to make an extraction of the intrinsic-k_T parameter q_s. To do this, we have implemented the predictions in numerical form using Monte Carlo computer codes, and performed fits to the data. The results of our work provide a determination of the non-perturbative q_s parameter as a function of the DY invariant mass, and of the soft-gluon resolution scale used in the parton branching evolution. While an extraction of q_s for fixed resolution scale has already been presented in the literature, an analysis with varying resolution scales has never been attempted before, so that the results presented here on this are entirely new.

To organize the presentation of our work, we have structured the thesis by starting with a brief introduction to the fundamental principles of particle physics and immediately jumping into the basic elements of Quantum Chromodynamics (QCD), the gauge field theory of the group SU(3) which describes the strong interaction between quarks and gluons. The goal of this part of the thesis is to describe how the partons (quarks and gluons) interact with each other inside hadrons in the Drell-Yan process. This is a process where high energetic hadrons collide with each other where a virtual photon or Z boson gets interchanged between the particles producing a lepton pair, for example two electrons. In our discussion of parton interactions, we have briefly described renormalization, renormalization group evolution equations, the running strong coupling α_s, the DGLAP evolution equations. Then we have proceeded to illustrate the Parton Branching-Transverse Momentum Distribution methodology, to find an expression for this equation that we can solve using a Monte Carlo method. Within this methodology we have presented the extraction of the intrinsic-k_T non-perturbative TMD parameter from fits to the measurements of Drell-Yan transverse momentum (p_T) differential cross sections performed at the LHC at 13 TeV, for Drell-Yan masses between 50 GeV and 1 TeV. This fitting was done using the Cascade3 program for the TMD evolution, and the MCatNLO program to obtain the Drell-Yan cross section in terms of the TMD distributions.

We made detailed studies and checks of our approach. The first aspect we examined was whether the number of events simulated in the Monte Carlo affects the data. This involves analyzing the number of LHE files used. We conducted simulations using both a small and a large set of LHE files. To determine if there is any dependence on this variable, we focused on the minimal uncertainty χ^2 (corresponding

to a specific q_s value). If this value remains consistent across different experimental setups, we can conclude that our program yields consistent results regardless of the variable used. We utilized two different q_0 values, and for $q_0 = 1.0$ GeV, it is evident from Figures 5.6 to 5.8 that the minimal uncertainty remains unchanged, regardless of the set used. However, examining the plots from 5.2 to 5.4, it is more challenging to confirm that these minimal χ^2 values match. Therefore, we continued to compare these values in the subsequent section. Upon reviewing Figure 5.15, we observe that the graphs for both sets closely resemble each other, leading us to conclude that the number of LHE files does not significantly impact the data. Nevertheless, there is another issue at play, specifically the recurring peak.

The reason for this peak is not entirely clear, but it could be associated with masses resembling that of the Z boson, which suggests that resonant production might be influencing the distributions. At resonance, the production cross-section is significantly enhanced, which could explain the observed peaks. For instance, if the resonance peak occurs at $q_0 = 0.5$ GeV, increasing q_0 might shift the energy distribution available for particle production, moving beyond the resonance or threshold energies where certain particles or states are more likely to be produced. Therefore, increasing q_0 could result in a distribution that either overshoots the resonance peak or affects the efficiency of detecting these states due to altered kinematics.

We also examined the influence of reducing the $p_{T,\text{max}}$ (thereby decreasing the number of data points) and found intriguing results. We employed $p_{T,\text{max}}$ values of 5, 10, and 15 GeV. For both q_0 values, we observed that at higher masses and higher q_s values, the uncertainty for $p_{T,\text{max}} = 5$ GeV becomes the lowest, while $p_{T,\text{max}} = 15$ GeV becomes the highest, despite the opposite being true at lower masses and q_s. This phenomenon could be attributed to the fact that at higher particle masses, using a lower maximum transverse momentum tends to yield more stable and reliable results. This setting helps to reduce unwanted background noise by filtering out less significant, lower momentum particles, thus allowing us to focus more on the significant signals emanating from higher mass particles.

We then wanted to determine if our calculations depend on these $p_{T,\text{max}}$ cuts. For $q_0 = 1.0$ GeV, the lines in Figure 5.19 closely match each other, indicating no dependence, which means we can achieve consistent results with fewer data points—a fascinating observation, especially from a numerical perspective. For $q_0 = 0.5$ GeV, a similar pattern emerges, although the well-known peak in Figure 5.15 complicates the analysis. However, if we disregard the peak, we observe a constant line (it slightly increases, likely due to systematic reasons.). The lines are also parallel to the x-axis, suggesting no (or mild) dependence on the mass of the lepton pair. Comparing Figure 5.15 with Figure 5.19, there appears to be a shift in the uncertainty value, which remains somewhat unclear. This could be because, at a lower q_0, the threshold for including emissions in the analysis is relatively low, allowing for a greater number of low-momentum emissions to contribute to the event. This typically results in a higher degree of background noise and potentially more fluctuations in the measured variables, which can lead to a relatively constant but noisy line in the data distribution.

Bibliography

[1] Wikipedia (n.d.), "Standard model", https://en.wikipedia.org/wiki/Standard_Model

[2] office of Science (n.d.), "DOE Explains Bosons and Fermions", https://www.energy.gov/science/doe-explainsbosons-and-fermions

[3] J. Tatum (n.d.), "Electron-Volts", https://phys.libretexts.org/Bookshelves/Electricity_and_Magnetism/Electricity_and_Magnetism_(Tatum)/

[4] University of Namur (n.d.), "Charge de l'atome", https://www.unamur.be/sciences/enligne/transition/chimie/fichesderevision/revision1/charge.htm

[5] P. Van. Mechelen (n.d.), "Subatomaire fysica", Retrieved from course notes from the subject 'Subatomic physics' at the University of Antwerp

[6] P. Van Mechelen (n.d.), "Inleiding Relativiteitstheorie en elementaire deeltjes", Retrieved from course notes from the subject 'Introduction Relativity theory and elementary particles' at the University of Antwerp

[7] CERN (n.d.), "Experiments", https://home.cern/science/experiments

[8] R.K. Ellis, W.J. Stirling and B.R. Webber (2003), "QCD and Collider Physics"

[9] CERN (n.d.), "CERN's accelerator complex", https://home.cern/science/accelerators/accelerator-complex

[10] K.G. Wilson (1974), "Confinement of Quarks", Phys. Rev. D10 2445

[11] M. E. Peskin and D. V. Schroeder (1995), "An introduction to Quantum Field Theory"

[12] D. Eelbode (n.d.), "Lie-groepen voor Fysici", Retrieved from course notes from the subject 'Lie groups for physicist' at the University of Antwerp

[13] F. Hautmann (2012), "An Introduction to QED & QCD", Retrieved from notes from lectures presented at the RAL High Energy Physics Summer School Somerville college, Oxford

[14] US Santa Cruz (2017), "Properties of the Gell-Mann matrices", https://scipp.ucsc.edu/~haber/archives/physics251_17/gellmann17.pdf

[15] W. O. Straub (2017), "A Child's Guide to Spinors", [viXra:1701.0299 [hep-lat]]

[16] A. D. Martin (2008),"Proton structure, Parton, QCD, DGLAP and beyond", [arXiv:0802.0161 [hep-ph]]

[17] University of Texas at Austin (n.d.), "Renormalization Scheme Dependence", https://web2.ph.utexas.edu/~vadim/Classes/2019s-qft/ms.pdf

[18] F. Hautmann, L. Keersmaekers, A. Lelek and A. M. Van Kampen, "Dynamical resolution

scale in transverse momentum distributions at the LHC", Nucl. Phys. B 949 (2019), 114795 [arXiv:1908.08524 [hep-ph]]

[19] The CMS collaboration, "Measurement of the mass dependence of the transverse momentumoflepton pairs in Drell–Yan production in proton-proton collisions at $\sqrt{s} = 13$ TeV", Eur. Phys. J. C 83 (2023), 628, [arXiv:2205.04897 [hep-ex]]

[20] F. Betchel (2009). "The Underlying Event in Proton-Proton Collisions", `https://cds.cern.ch/record/1446555`

[21] F. Hautmann, H. Jung, A. Lelek, V. Radescu and R. Zlebcik, "Collinear and TMD Quark and Gluon Densities from Parton Branching Solution of QCD Evolution Equations", JHEP 01 (2018), 070, [arXiv:1708.03279 [hep-ph]]

[22] R. Hamberg, T. Matsuura and W.L. van Neerven, "Nucl. Phys. B345"; ibid (1991), *B359*

[23] S. Baranov, A. Bermudez Martinez, L.I. Estevez Banos, F. Guzman, F. Hautmann, H. Jung, A. Lelek, J. Lidrych, A. Lipatov, M. Malyshev, M. Mendizabal, S. Taheri Monfared, A.M. van Kampen, Q. Wang, H. Yang. "A Monte Carlo even generator based on TMDs", Eur. Phys. J. C 81 (2021), 425 [arXiv:2101.10221 [hep-ph]]

[24] A. Bermudez Martinez, P. Connor, H. Jung, A. Lelek, R. Žlebčík, F. Hautmann and V. Radescu, "Collinear and TMD parton densities from fits to precision DIS measurements in the parton branching method", Phys. Rev. D 99 (2019) no.7, 074008 [arXiv:1804.11152 [hep-ph]]

[25] A. Bermudez Martinez *et al.*, "Production of Z-bosons in the parton branching method", Phys. Rev. D100 (2019) 074027 [arXiv:1906.00919].

[26] A. Bermudez Martinez et al., "The transverse momentum spectrum of low mass Drell-Yan production at next-to-leading order in the parton branching method", Eur. Phys. J. C 80 (2020) 598 [arXiv:2001.06488].

[27] J. Alwall et al., "The automated computation of tree-level and next-to-leading order differential cross sections, and their matching to parton shower simulations", JHEP 1407 (2014) 079 [arXiv:1405.0301].

[28] R. Angeles-Martinez et al., "Transverse Momentum Dependent (TMD) parton distribution functions: status and prospects", Acta Phys. Polon. B46 (2015) 2501 [arXiv:1507.05267].

[29] F. Hautmann et al., "Soft-gluon resolution scale in QCD evolution equations", Phys. Lett. B 772 (2017) 446 [arXiv:1704.01757].

[30] H. Yang *et al.*, "Back-to-back azimuthal correlations in Z + jet events at high transverse momentum in the TMD parton branching method at next-to-leading order", Eur. Phys. J. C **82** (2022) 755 [arXiv:2204.01528 [hep-ph]].

[31] S. Dooling *et al.*, "Longitudinal momentum shifts, showering, and nonperturbative corrections in matched next-to-leading-order shower event generators", Phys. Rev. D87 (2013) 094009 [arXiv:1212.6164 [hep-ph]].

[32] S. Dooling *et al.*, "Nonperturbative corrections and showering in NLO-matched event generators", arXiv:1304.7180 [hep-ph].

[33] F. Hautmann and H. Jung, "Collinearity approximations and kinematic shifts in partonic shower algorithms", Eur. Phys. J. C72 (2012) 2254 [arXiv:1209.6549].

[34] S. Baranov et al., “CASCADE3 A Monte Carlo event generator based on TMDs”, Eur. Phys. J. C81 (2021) 425 [arXiv:2101.10221].

[35] H. Jung et al., “The CCFM Monte Carlo generator CASCADE version 2.2.03”, Eur. Phys. J. C70 (2010) 1237 [arXiv:1008.0152].

[36] M. I. Abdulhamid et al., “Azimuthal correlations of high transverse momentum jets at next-to-leading order in the parton branching method”, Eur. Phys. J. C82 (2022) 36 [arXiv:2112.10465].

[37] A. Bermudez Martinez and F. Hautmann, “Azimuthal di-jet correlations with parton branching TMD distributions”, arXiv:2208.08446 [hep-ph].

[38] A. Bermudez Martinez, F. Hautmann and M. L. Mangano, “TMD evolution and multi-jet merging,” Phys. Lett. B **822** (2021) 136700 [arXiv:2107.01224 [hep-ph]].

[39] A. Bermudez Martinez, F. Hautmann and M. L. Mangano, “Multi-jet physics at high-energy colliders and TMD parton evolution,” arXiv:2109.08173 [hep-ph].

[40] A. Bermudez Martinez, F. Hautmann and M. L. Mangano, “Multi-jet merging with TMD parton branching,” JHEP **09** (2022) 060 [arXiv:2208.02276 [hep-ph]].

[41] S. Sadeghi Barzani, “PB TMD fits at NLO with dynamical resolution scale”, arXiv:2207.13519 [hep-ph].

[42] ZEUS, H1 Collaboration, “Combination of measurements of inclusive deep inelastic ep scattering cross sections and QCD analysis of HERA data”, Eur. Phys. J. C75 (2015) 580 [arXiv:1506.06042].

[43] xFitter Developers’ Team Collaboration, H. Abdolmaleki et al., “xFitter: An Open Source QCD Analysis Framework. A resource and reference document for the Snowmass study”, arXiv:2206.12465.

[44] S. Alekhin et al., “HERAFitter”, Eur. Phys. J. C75 (2015) 304 [arXiv:1410.4412].

[45] I. Bubanja, A. Bermudez Martinez, L. Favart, F. Guzman, F. Hautmann, H. Jung, A. Lelek, M. Mendizabal, K. M. Figueroa and L. Moureaux, *et al.* ”The small k_{T}region in Drell–Yan production at next-to-leading order with the parton branching method”, Eur. Phys. J. C 84 (2024) no.2, 154, [arXiv:2312.08655 [hep-ph]]

[46] J. C. Collins, D. E. Soper, and G. F. Sterman, “Transverse Momentum Distribution in Drell-Yan Pair and W and Z Boson production”, Nucl.Phys. B250 (1985) 199.

[47] A. Bacchetta et al., “Flavor dependence of unpolarized quark transverse momentum distributions from a global fit”, JHEP 08 (2024) 232 [arXiv:2405.13833 [hep-ph]].

[48] A. Bacchetta et al., “Unpolarized transverse momentum distributions from a global fit of Drell-Yan and semi-inclusive deep-inelastic scattering data”, JHEP 10 (2022) 127 [arXiv:2206.07598 [hep-ph]].

[49] M. Bury et al., “PDF bias and flavor dependence in TMD distributions”, JHEP 10 (2022) 118 [arXiv:2201.07114 [hep-ph]].

[50] M. Bury et al., “Flavor dependent b-profiles from Drell-Yan spectra at low transverse momenta,” PoS **ICHEP2022** (2022) 834 [arXiv:2211.05063 [hep-ph]].

[51] F. Hautmann, I. Scimemi and A. Vladimirov, “Non-perturbative contributions to vector-

boson transverse momentum spectra in hadronic collisions," Phys. Lett. B **806** (2020) 135478 [arXiv:2002.12810 [hep-ph]].

[52] F. Hautmann, I. Scimemi and A. Vladimirov, "Determination of the rapidity evolution kernel from Drell-Yan data at low transverse momenta," SciPost Phys. Proc. **8** (2022) 123 [arXiv:2109.12051 [hep-ph]].

[53] N. A. Abdulov et al., "TMDlib2 and TMDplotter: a platform for 3D hadron structure studies", Eur. Phys. J. C81 (2021) 752, [arXiv:2103.09741].

[54] F. Hautmann et al., "TMDlib and TMDplotter: library and plotting tools for transverse-momentum-dependent parton distributions", Eur. Phys. J. C74 (2014) 3220 [arXiv:1408.3015].

[55] A. Bermudez Martinez et al., "The Parton Branching Sudakov and its relation to CSS", PoS **EPS-HEP2023** (2024) 270.

[56] Pythia (n.d.). "Les Houches Event files", `https://pythia.org/latest-manual/LHEF.html#section0`

[57] Open University (n.d.). "W and Z bosons", `https://www.open.edu/openlearn/science-maths-technology/particle-physics`